

# Misspecification-robust amortised simulation-based inference using variational methods

Matthew O’Callaghan

*Institute of Astronomy, University of Cambridge*

*mo503@cam.ac.uk*

Kaisey S. Mandel

*Institute of Astronomy, University of Cambridge*

*Statistical Laboratory, University of Cambridge*

*Kavli Institute for Cosmology, University of Cambridge*

Gerry Gilmore

*Institute of Astronomy, University of Cambridge*

*Institute of Astrophysics, FORTH*

## Abstract

Recent advances in neural density estimation have enabled powerful simulation-based inference (SBI) methods that can flexibly approximate Bayesian inference for intractable stochastic models. Although these methods have demonstrated reliable posterior estimation when the simulator accurately represents the underlying data generative process (DGP), recent work has shown that they perform poorly in the presence of model misspecification. This poses a significant issue for their use in real-world problems, due to simulators *always* misrepresenting the true DGP to a certain degree. In this paper, we introduce robust variational neural posterior estimation (RVNP), a method which addresses the problem of misspecification in amortised SBI by bridging the simulation-to-reality gap using variational inference and error modelling. We test RVNP on multiple benchmark tasks, including using real data from astronomy, and show that it can recover robust posterior inference in a data-driven manner without adopting hyperparameters or priors governing the misspecification influence.

## 1 Introduction

Simulator models are ubiquitous in many areas of the natural sciences and engineering, enabling researchers to approximate complex real-world data generative processes (DGP) using physically grounded forward models. However, these simulators are often computationally expensive, non-differentiable, and lack closed-form likelihoods, making traditional inference methods inapplicable. Implicitly, the simulator defines an intractable likelihood  $p(\mathbf{x}_{\text{sim}}|\boldsymbol{\theta})$  over  $\mathcal{X}_{\text{sim}} \subseteq \mathbb{R}^n$ , relating the simulated observations and the parameters of interest  $\boldsymbol{\theta} \in \Theta \subseteq \mathbb{R}^m$ . As a result of intractability and the computational expense of running simulations, solving the inverse problem of inferring simulator parameters from observed data  $\mathbf{x}_{\text{obs}}$  poses a significant challenge. Simulation-based inference (SBI, Cranmer et al. 2020) or *likelihood-free inference* provides methods to approximately infer the posterior distribution of the simulator parameters conditioned on observed data.

A range of SBI methods have emerged to solve the likelihood-free inference problem, beginning with traditional approaches such as approximate Bayesian computation (ABC; Rubin 1984; Beaumont et al. 2002) and Bayesian synthetic likelihood (BSL, Price et al. 2018). Recent work has introduced methods based on neural density estimation, such as neural posterior estimation (NPE, Papamakarios & Murray 2016; Lueckmann et al. 2017; Greenberg et al. 2019), neural likelihood estimation (NLE, Lueckmann et al. 2019; Papamakarios et al. 2019), neural ratio estimation (NRE, Izbicki et al. 2014; Cranmer et al. 2016; Hermans et al. 2020;

---

Durkan et al. 2020), and modelling the joint distribution of data and simulation parameters (Glöckler et al., 2024). SBI methods can be categorised into *amortised* and *non-amortised* inference methods. In the context of neural SBI, non-amortised methods such as sequential neural posterior estimation (SNPE; Papamakarios & Murray 2016; Lueckmann et al. 2017; Greenberg et al. 2019), sequential neural likelihood estimation (SNLE; Papamakarios et al. 2019), and sequential neural ratio estimation (SNRE; Hermans et al. 2020) target a single posterior conditioned on fixed data, adapting their inference procedure with each simulation round. After an up-front simulation budget, amortised methods aim to learn a global inference model over a given prior, making them well-suited for scenarios where repeated or scalable inference is required. In this paper, we focus on SBI methods for inferring posterior distributions that are amortised over a dataset of observations.

SBI methods have been widely used in fields such as astronomy (Mishra-Sharma & Cranmer, 2022), particle physics (The Atlas Collaboration, 2025), cosmology (Lemos et al. 2023; Zeghal et al. 2024), and neuroscience (Oesterle et al. 2020; Hashemi et al. 2024), to name a few. However, recent work has shown that they can yield overconfident posterior approximations (Hermans et al., 2022) and suffer significantly when the true DGP does not lie within the family of distributions defined by the statistical model (Cannon et al. 2022; Schmitt et al. 2024), known as *model misspecification*. Model misspecification may be caused by a variety of factors, such as contamination in the data or unaccounted-for physical processes in the modelling that can lead to *overconfident* posteriors (Hermans et al., 2022). This discrepancy between the simulated data and the real observations is known as the *simulation-to-reality gap* (Miglino et al., 1995) or simulation gap.

Methods for mitigating against misspecification in neural SBI have done so mainly by addressing the simulation-to-reality gap. This is based on the assumption that misspecification appears as a divergence-based discrepancy between the true DGP  $p^*(\mathbf{x}_{\text{obs}})$  and the marginal distribution described by the simulator model  $p(\mathbf{x}_{\text{sim}}) = \mathbb{E}_{p(\boldsymbol{\theta})}[p(\mathbf{x}_{\text{sim}}|\boldsymbol{\theta})]$ , under the prior distribution  $p(\boldsymbol{\theta})$ . Robust SBI methods often address the simulation-to-reality gap through error modelling and adjustment parameters (Ward et al. 2022; Frazier & Drovandi 2021; Kelly et al. 2024), domain adaptation approaches (Huang et al. 2023; Swierc et al. 2024; Elsemüller et al. 2025; Mishra et al. 2025), or generalised Bayesian inference (Dellaporta et al., 2022). The success of most of these methods relies on the observed points appearing as out-of-distribution (OOD) with respect to the simulated observations. However, recent work has underscored the importance of within-distribution (ID) points in a misspecified SBI (Schmitt et al., 2024; Frazier et al., 2024; Elsemüller et al., 2025), as the errors in the model may still produce summary statistics which lie ID relative to the simulations. Wehenkel et al. (2025) showed that using a reliable calibration set can aid towards robust amortised SBI under such modelling errors. Often, a reliable calibration set will not exist, making such problems highly difficult to solve. Recently, unsupervised domain adaptation (UDA) methods have been implemented in robust amortised SBI using maximum mean discrepancy (MMD), domain-adversarial neural networks (Elsemüller et al., 2025), and consistency loss regularisation (Mishra et al., 2025). As amortised SBI looks to construct general posteriors for a range of observations, it is natural to consider the misspecification problem for situations involving many observations where all points appear OOD, or when a significant number of points appear OOD.

Despite their success in robust SBI, existing methods encounter issues in the context of robust *amortised* SBI. In particular, the error modelling and correction parameter approaches scale poorly to amortised Bayesian inference due to their dependence on a Markov Chain Monte Carlo (MCMC) sampling step. On the other hand, they benefit from their Bayesian formulation, particularly through the connection between hyperparameter choice and Bayesian prior adoption (Ward et al. 2022; Frazier & Drovandi 2021; Kelly et al. 2024). Domain adaptation methods scale more favourably to amortised SBI, but come at the cost of a non-Bayesian interpretation of the domain adaptation hyperparameters, a lack of interoperability of the domain adaptation (Elsemüller et al., 2025), and a lack of clarity between the trade-off in the domain adaptation and the inference algorithm (Chen et al., 2021). Furthermore, it is not always desirable to use domain-adapted neural embedding statistics if expert knowledge on the summary embedding space is available, such as known sufficient statistics on a low-dimensional observation space in physically motivated units. Data-driven methods that have a reliable Bayesian interpretation and do not rely on hyperparameters are desirable in this context.

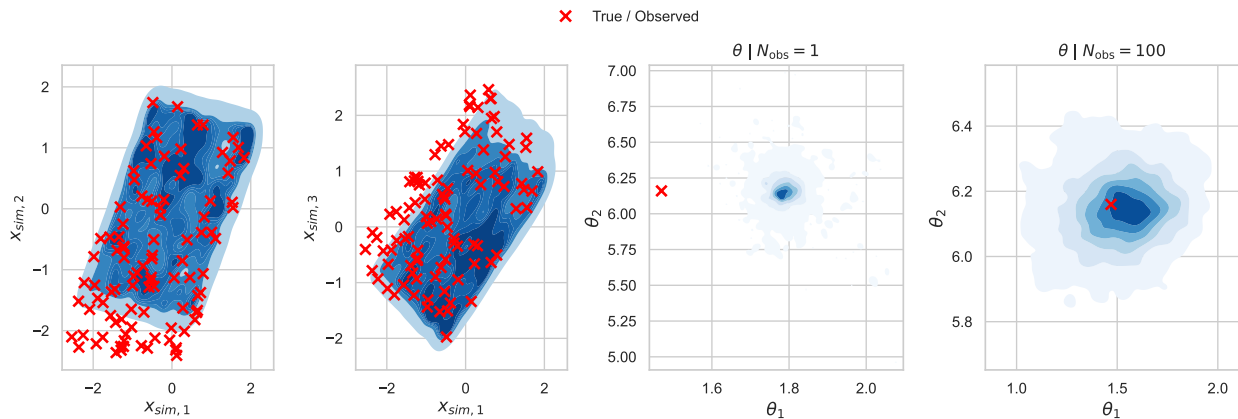


Figure 1: Summary statistics for the pendulum task, where many of the misspecified observations (red) will appear within high-probability regions of the marginal density  $p(\mathbf{x}_{\text{sim}})$  (underlying hue). Multiple observations will provide information on the simulation-to-reality gap for the pendulum task. Furthermore, it highlights the issue of fitting for the misspecification using a single observation that, if it appears within the distribution, will contain no information about the misspecification. The two right-most images show that by increasing the number of observations, we recover a more reliable inference.

## 1.1 Our contributions

**Problem setting:** Given a dataset  $\mathcal{O} = \{\mathbf{x}_{\text{obs}}^{(i)}\}_{i=1}^{N_{\text{obs}}}$  where each observation corresponds to a different unknown parameter  $\theta^{*(i)}$ , we seek to infer all posterior distributions  $\{p(\theta | \mathbf{x}_{\text{obs}}^{(i)})\}_{i=1}^{N_{\text{obs}}}$ , when the simulator model is misspecified.

**Amortised SBI:** In this paper, we refer to amortised SBI as amortising the Bayesian inference over all data points in  $\mathcal{O}$ . This definition is in line with amortised variational inference (Margossian & Blei, 2023).

**Our solution:** We propose robust variational neural posterior estimation (RVNP) and its tuned variant (RVNP-T), methods that address the misspecification problem in amortized SBI. RVNP pre-trains a simulator likelihood  $p_{\Psi}(\mathbf{x}_{\text{sim}} | \theta)$ , adopts a flexible error model  $p_{\alpha}(\mathbf{x}_{\text{obs}} | \mathbf{x}_{\text{sim}}, \theta)$ , and uses an importance weighted autoencoder (Burda et al., 2015) inference scheme to maximize the evidence of the true data under the variational posterior  $q_{\phi}(\theta | \mathbf{x}_{\text{obs}})$  for the parameters  $\alpha$  and  $\phi$ .

The **main claim** of our paper is that RVNP and its tuned variant can recover robust amortised posterior inference under misspecification by bridging the simulation-to-reality gap using error modelling. The error model parameters are adapted in a data-driven way when we have many observations and the method requires no extra manually tuned *misspecification-related* hyperparameters or priors that govern the influence of the misspecification. We summarise our contributions as follows:

1. We introduce RVNP, an amortised SBI method that uses a pre-trained simulator likelihood, an error model, and an importance-weighted autoencoder (Burda et al., 2015) scheme to return robust amortised posterior inference under misspecification without adopting user-tuned misspecification-related hyperparameters or priors. We also introduce RVNP-T, which tunes the final posterior using the simulator and the noise induced by the error model.
2. We investigate the effect of the number of observed data points on error modelling in robust SBI for the first time.
3. To our knowledge, this is the first example of using amortised variational inference to address the misspecification problem in SBI.

**Overview of Paper.** In Section 2, we provide an overview of the background necessary for the paper. Section 3 describes the methods that will be applied to experiments in Section 4. In Section 5, we discuss related works. We conclude the paper in Section 6 with a discussion and conclusion.

## 2 Background

### 2.1 SBI formalism

Let  $\theta \in \Theta \subseteq \mathbb{R}^m$  be the **target parameters** of interest which are to be inferred after adopting a prior distribution  $p(\theta)$ .

Let  $\mathbf{x}_{\text{sim}} \in \mathcal{X}_{\text{sim}} \subseteq \mathbb{R}^n$  denote a **simulated observation**. The **simulator** is a family of distributions parametrized by  $\theta$  which can be represented by an unknown density  $p(\mathbf{x}_{\text{sim}}|\theta)$  over  $\mathcal{X}_{\text{sim}}$ , relating the simulated observations and the parameters of interest  $\theta \in \mathbb{R}^m$ .

We denote  $\mathbf{x}_{\text{obs}} \in \mathcal{X}_{\text{obs}} \subseteq \mathbb{R}^n$  as a **true observation** and  $\theta^* \in \mathbb{R}^m$  as the **ground truth** of the parameter  $\theta$  for an experiment. We let  $p^*(\mathbf{x}_{\text{obs}})$  denote the true, unknown, DGP.

We define the **error model** as  $p_{\alpha}(\mathbf{x}_{\text{obs}}|\mathbf{x}_{\text{sim}}, \theta)$ , a family of distributions parametrized by  $\alpha \in \mathbb{R}^k$ ,  $\mathbf{x}_{\text{sim}}$ , and  $\theta$ , which relates the simulations to observations.

We assume that we have  $D = \{\theta^{(i)}, \mathbf{x}_{\text{sim}}^{(i)}\}_{i=1}^{N_{\text{sim}}}$ , a fixed number of points generated from the synthetic DGP  $p(\mathbf{x}_{\text{sim}}|\theta)p(\theta)$ , and a set of observations,  $O = \{\mathbf{x}_{\text{obs}}^{(i)}\}_{i=1}^{N_{\text{obs}}}$  each associated to a different, unknown true  $\theta^*$  value.

We let  $\iota_{\omega} : \mathbb{R}^n \rightarrow \mathbb{R}^l$ ,  $\mathbf{x}_{\text{sim}} \mapsto \mathbf{z}_{\text{sim}}$  denote a **statistical embedding** parametrized by  $\omega$ . This embedding can represent fixed user-defined summary statistics, a pre-defined embedding, or a neural statistic estimator (NSE) where the parameters  $\omega$  are to be learnt. Lower-dimensional embeddings are important when dealing with high-dimensional data, but can come at the cost of information loss when the embedding is not a sufficient statistic of  $\mathbf{x}_{\text{sim}}$  for  $\theta$  (Blum et al., 2013). In this paper, we consider examples where we have expert-informed summary statistics, and neural embedding summary statistics.

### 2.2 Amortised neural posterior and neural likelihood estimation

The goal of amortised neural posterior estimation is to approximate the unknown posterior distribution  $p^*(\theta|\mathbf{x}_{\text{obs}})$  for all  $\mathbf{x}_{\text{obs}} \in \mathcal{X}_{\text{obs}}$ . After choosing a conditional density estimation architecture  $q_{\phi}(\theta|\mathbf{x}_{\text{obs}})$  parametrized by  $\phi$ , and an architecture for the neural statistic embedding,  $\iota_{\omega}$ , NPE (Papamakarios & Murray 2016; Lueckmann et al. 2017; Greenberg et al. 2019) fits for the parameters  $\omega$  and  $\phi$  by minimizing the the expected forward Kullback-Leibler (KL) divergence between analytic and approximate posterior

$$\mathbb{E}_{p^*(\mathbf{x}_{\text{obs}})}[\text{KL}[p(\theta|\mathbf{x}_{\text{obs}})||q_{\phi}(\theta|\iota_{\omega}(\mathbf{x}_{\text{obs}}))]], \quad (1)$$

where the expectation is over the unknown true data-generating distribution  $p^*(\mathbf{x}_{\text{obs}})$ . Minimizing this is equivalent to minimizing the NPE loss function

$$\mathcal{L}_{\text{NPE}}(\phi, \omega) = \mathbb{E}_{p^*(\mathbf{x}_{\text{obs}})}[\mathbb{E}_{p(\theta|\mathbf{x}_{\text{obs}})}[-\log q_{\phi}(\theta|\mathbf{x}_{\text{obs}})]], \quad (2)$$

since the true unknown posterior and its entropy do not depend on the trainable neural network parameters.

This amortised posterior objective function is not realistic in most situations (Schmitt et al., 2024), as we rarely have enough real data to approximate the expectation with respect to  $p^*(\mathbf{x}_{\text{obs}})$ , and the true posterior is unknown. Instead, the unknown  $p^*(\mathbf{x}_{\text{obs}})$  is replaced by the marginal likelihood  $p(\mathbf{x}_{\text{obs}}) = \int p(\mathbf{x}_{\text{obs}}|\theta)p(\theta)d\theta$ . Under this assumption that there is no misspecification,  $\mathbf{x}_{\text{obs}}$  can be replaced with  $\mathbf{x}_{\text{sim}}$  and the objective becomes

$$\mathcal{L}(\phi, \omega)_{\text{NPE}} := -\mathbb{E}_{\mathbf{x}_{\text{sim}}, \theta}[\log q_{\phi}(\theta|\iota_{\omega}(\mathbf{x}_{\text{sim}}))], \quad (3)$$

where the expectation is over simulator input and output pairs. This is minimised with respect to the parameters  $\omega$  and  $\phi$ . The success of this objective depends on the assumption that sampling from the evidence is equivalent to sampling from  $p^*(\mathbf{x}_{\text{obs}})$ .

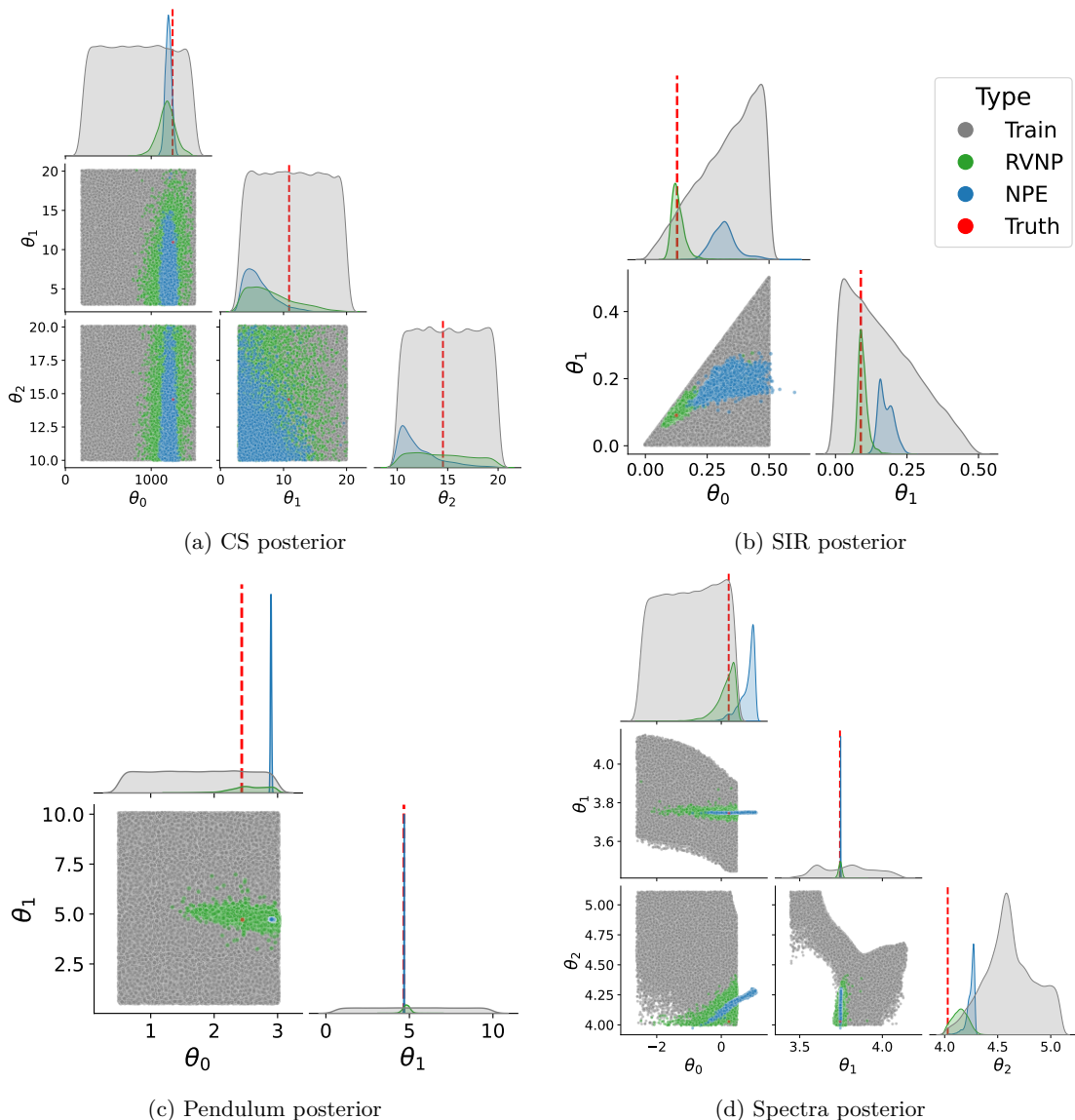


Figure 2: Samples from posterior distribution conditional on a single observed point when RVNP was trained on  $N_{\text{obs}} = 1000$  different observations. The green corresponds to RVNP, the blue corresponds to NPE, and the red point (dashed line) corresponds to the true  $\theta^*$ . The grey corresponds to the training samples. We see that RVNP is significantly more robust than NPE, particularly in the complex pendulum and spectra task.

Neural likelihood estimation (NLE) learns a distribution maximising the conditional log-probability of the simulated data

$$\mathcal{L}(\Psi)_{\text{NLE}} := \mathbb{E}_{p(\mathbf{x}_{\text{sim}}|\theta)p(\theta)}[\log p_{\Psi}(\iota_{\omega}(\mathbf{x}_{\text{sim}})|\theta)] \quad (4)$$

with respect to the flow parameters  $\Psi$ , which is equivalent to minimising the KL divergence between the flow and the target distribution. The parameters for the neural summary statistics must be implemented in a two-stage manner because it cannot be trained in an end-to-end fashion along with the likelihood proxy (Brehmer & Cranmer, 2020). Sampling from the posterior amounts to adopting either a Markov Chain Monte Carlo (MCMC) sampling method or a variational inference algorithm, which will increase the number of architecture choices and hyperparameter tuning, but can recover accurate posterior inference (Glöckler et al., 2022).

### 2.3 Misspecification in SBI

The simulator,  $p(\mathbf{x}_{\text{sim}}|\boldsymbol{\theta})$ , is said to be misspecified if the true data generative process does not fall within the family of distributions defined by the simulator on the support of the prior of  $\boldsymbol{\theta}$ . That is,  $p^* \notin \{p(\mathbf{x}_{\text{sim}}|\boldsymbol{\theta}); \boldsymbol{\theta} \in \Theta\}$  (Cannon et al., 2022). In this paper, we adopt the adjusted definition of misspecification provided in Wehenkel et al. (2025), which is more aligned with amortised SBI. They define a simulator to be misspecified if  $\exists \mathcal{S} \subseteq \Theta \times \mathcal{X}_{\text{obs}} : \forall (\boldsymbol{\theta}, \mathbf{x}_{\text{obs}}) \in \mathcal{S}$

$$p(\boldsymbol{\theta}) = p^*(\boldsymbol{\theta}) \text{ and } p^*(\boldsymbol{\theta}|\mathbf{x}_{\text{obs}}) \neq p(\boldsymbol{\theta}|\mathbf{x}_{\text{sim}} = \mathbf{x}_{\text{obs}}). \quad (5)$$

This definition aligns with the amortised SBI task as it identifies misspecification as a set-wise phenomenon. Our goal is to recover robust and reliable posterior inference for all  $\mathbf{x}_{\text{obs}} \in \mathcal{X}_{\text{obs}}$ . This definition does, however, ignore situations when the prior distribution is misspecified. Prior misspecification is addressed at the end of the paper in the discussion.

### 2.4 Importance weighted autoencoders

Importance-weighted autoencoders (IWAE) were inspired by the vanilla variational autoencoder (VAE, Kingma & Welling 2013), which introduces a latent space  $\Theta \subseteq \mathbb{R}^m$  and two distributions,  $p_{\boldsymbol{\alpha}}(\mathbf{x}|\boldsymbol{\theta})$  and  $q_{\boldsymbol{\phi}}(\boldsymbol{\theta}|\mathbf{x})$ , known as the decoder and the encoder respectively. The vanilla VAE aims to maximise the evidence of the data using the evidence lower bound

$$\log p(\mathbf{x}) \geq \mathbb{E}_{q_{\boldsymbol{\phi}}(\boldsymbol{\theta}|\mathbf{x})} [\log p_{\boldsymbol{\alpha}}(\mathbf{x}|\boldsymbol{\theta})] - \text{KL}(q_{\boldsymbol{\phi}}(\boldsymbol{\theta}|\mathbf{x}) \| p(\boldsymbol{\theta})) \quad (6)$$

with respect to  $\boldsymbol{\alpha}$  and  $\boldsymbol{\phi}$ , where  $p(\boldsymbol{\theta})$  is a prior over the latent parameter. However, using this bound has been shown to induce mode-seeking behaviour, leading to overly simplified representations and poor inference. Burda et al. (2015) introduced IWAE, which is based on a strictly tighter evidence lower bound derived from importance sampling. The log-evidence for a single point is given as

$$\log p_{\boldsymbol{\theta}}(\mathbf{x}) \approx \log \left[ \frac{1}{k} \sum_{l=1}^k \frac{p_{\boldsymbol{\alpha}}(\mathbf{x}, \boldsymbol{\theta}^{(l)})}{q_{\boldsymbol{\phi}}(\boldsymbol{\theta}^{(l)}|\mathbf{x})} \right] = \mathcal{L}_k^{\text{IWAE}}(\boldsymbol{\alpha}, \boldsymbol{\phi}; \mathbf{x}) \quad (7)$$

$$\text{with } \boldsymbol{\theta}^{(l)} \sim q_{\boldsymbol{\phi}}(\boldsymbol{\theta}|\mathbf{x}), \quad (8)$$

which is a mass-covering objective that targets the evidence. We use the The doubly reparameterized gradient (DReG) estimator (Tucker et al., 2018) to avoid low signal-to-noise in the gradient estimation.

Cremer et al. (2017) proposed using the implicit distribution given by importance sampling from the true posterior using the variational posterior as a proposal distribution. Given samples  $\boldsymbol{\theta}_{2:N_s} := \boldsymbol{\theta}_2, \dots, \boldsymbol{\theta}_{N_s}$ , they define the implicit distribution arising from importance sampling as

$$\tilde{q}_{IW}(\boldsymbol{\theta}|\mathbf{x}, \boldsymbol{\theta}_{2:N_s}) := \frac{p(\mathbf{x}, \boldsymbol{\theta})}{\frac{1}{N_s} \left( \frac{p(\mathbf{x}, \boldsymbol{\theta})}{q_{\boldsymbol{\phi}}(\boldsymbol{\theta}|\mathbf{x})} + \sum_{k=1}^{N_s} \frac{p(\mathbf{x}, \boldsymbol{\theta}_k)}{q_{\boldsymbol{\phi}}(\boldsymbol{\theta}_k|\mathbf{x})} \right)}, \quad (9)$$

which has the property that

$$q_{\text{SIR}}(\boldsymbol{\theta}|\mathbf{x}) := \mathbb{E}_{\boldsymbol{\theta}_{2:N_s}} [\tilde{q}_{IW}(\boldsymbol{\theta}|\mathbf{x}, \boldsymbol{\theta}_{2:N_s})] \rightarrow p(\boldsymbol{\theta}|\mathbf{x}), \text{ when } N_s \rightarrow \infty \quad (10)$$

the expectation of the implicit distribution approaches the true posterior. Sampling from this distribution is detailed explicitly in Cremer et al. (2017), and is done by sampling-importance-resampling (SIR).

## 3 Method: RVNP

Motivated by a desire to have a method that can recover robust amortised posterior inference with a fixed embedding space such that the simulation-to-reality gap is bridged with an interpretable, flexible, and data-driven error model, we extend neural likelihood estimation and the error modelling approaches for model

misspecification (Ward et al., 2022; Kelly et al., 2024) to amortised SBI and propose robust variational neural posterior estimation (RVNP). RVNP builds on variational methods for solving the inverse problem under a learnt likelihood in SBI (Glöckler et al., 2022) by adopting an importance weighted autoencoder amortised variational inference scheme (Burda et al., 2015) to define robust variational neural posterior estimation (RVNP) and its tuned variant (RVNP-T).

In what follows, we drop the explicit embedding notation  $\iota_\omega$  unless necessary. Our goal is to use a normalising flow parametrized by  $\phi$ ,  $q_\phi(\boldsymbol{\theta} | \mathbf{x}_{\text{obs}})$ , that can approximate the true posterior distribution in an amortised manner. Algorithm 1 provides an overview of the RVNP and RVNP-T algorithms.

### 3.1 Generative model

Throughout, we assume a pre-training or fixing of the neural statistic embedding  $\iota_\omega : \mathbb{R}^n \rightarrow \mathbb{R}^l$  occurred. The first step of RVNP is to train the normalising flow  $p_\Psi(\mathbf{x} | \boldsymbol{\theta})$  to approximate the likelihood using the generated samples from the simulator by minimising the NLE objective (Equation 4). Once the normalising flow has been trained, we assume that  $p(\mathbf{x}_{\text{sim}} | \boldsymbol{\theta}) \approx p_\Psi(\mathbf{x}_{\text{sim}} | \boldsymbol{\theta})$  and include the surrogate in the forward model. We assume that the true DGP can be modelled as

1.  $p(\boldsymbol{\alpha})$  a prior over the error model weights.
2.  $\boldsymbol{\theta} \sim p(\boldsymbol{\theta})$ , where  $p(\boldsymbol{\theta})$  is known and tractable.
3.  $\mathbf{x}_{\text{sim}} \sim p_\Psi(\mathbf{x}_{\text{sim}} | \boldsymbol{\theta})$ .
4.  $\mathbf{x}_{\text{obs}} \sim p_\alpha(\mathbf{x}_{\text{obs}} | \mathbf{x}_{\text{sim}}, \boldsymbol{\theta})$ , where  $p_\alpha(\mathbf{x}_{\text{obs}} | \mathbf{x}_{\text{sim}}, \boldsymbol{\theta}) = \mathcal{N}(\mathbf{x}_{\text{obs}}; \mathbf{x}_{\text{sim}}, \boldsymbol{\xi}(\boldsymbol{\theta}; \boldsymbol{\alpha}))$  is an adopted error model where the covariance matrix is the output of a neural network  $\text{NN}(\boldsymbol{\theta})$  parametrized by  $\boldsymbol{\alpha}$ .

We assume that the observed data  $\mathbf{x}_{\text{obs}}^{(i)}$  are conditionally independent given their latent parameters  $\boldsymbol{\theta}^{(i)}$  and the error model parameters  $\boldsymbol{\alpha}$ . Under this generative model, the posterior distribution is proportional to

$$p(\{\boldsymbol{\theta}^{(i)}\}_{i=1}^{N_{\text{obs}}}, \boldsymbol{\alpha} | O) \propto p(\boldsymbol{\alpha}) \prod_{i=1}^{N_{\text{obs}}} \int p_\alpha(\mathbf{x}_{\text{obs}} | \mathbf{x}_{\text{sim}}, \boldsymbol{\theta}) p_\Psi(\mathbf{x}_{\text{sim}}^{(i)} | \boldsymbol{\theta}^{(i)}) p(\boldsymbol{\theta}^{(i)}) d\mathbf{x}_{\text{sim}}^{(i)}. \quad (11)$$

### 3.2 Variational posterior

From the posterior distribution of our forward model (Equation 11), we can express the log-evidence of the data as

$$\log p(O) = \sum_{i=1}^{N_{\text{obs}}} \log \mathbb{E}_{p(\boldsymbol{\theta}^{(i)})} \mathbb{E}_{p_\Psi(\mathbf{x}_{\text{sim}}^{(i)} | \boldsymbol{\theta}^{(i)})} [p_\alpha(\mathbf{x}_{\text{obs}}^{(i)} | \mathbf{x}_{\text{sim}}^{(i)}, \boldsymbol{\theta}^{(i)})] + \log p(\boldsymbol{\alpha}). \quad (12)$$

We can use the IWAE lower bound on the log-evidence (Equation 7) to derive the variational loss function for RVNP as

$$\mathcal{L}(\phi, \boldsymbol{\alpha})_V \approx - \sum_{i=1}^{N_{\text{obs}}} \log \left[ \frac{1}{K} \sum_{l=1}^K \frac{\mathbb{E}_{p_\Psi(\mathbf{x}_{\text{sim}} | \boldsymbol{\theta}^{(i)})} [p_\alpha(\mathbf{x}_{\text{obs}}^{(i)} | \mathbf{x}_{\text{sim}}^{(i)}, \boldsymbol{\theta}^{(l)})] p(\boldsymbol{\theta}^{(l)})}{q_\phi(\boldsymbol{\theta}^{(l)} | \mathbf{x}_{\text{obs}}^{(i)})} \right] - \log p(\boldsymbol{\alpha}) \quad (13)$$

where  $\boldsymbol{\theta}^{(l)} \sim q_\phi(\boldsymbol{\theta} | \mathbf{x}_{\text{obs}}^{(i)})$ , and for each  $\boldsymbol{\theta}^{(l)}$  we approximate  $\mathbb{E}_{p_\Psi(\mathbf{x}_{\text{sim}} | \boldsymbol{\theta}^{(l)})} [p_\alpha(\mathbf{x}_{\text{obs}}^{(i)} | \mathbf{x}_{\text{sim}}^{(i)}, \boldsymbol{\theta}^{(l)})]$  using a Monte Carlo (MC) estimate. We use the `logsumexp` function to ensure the MC estimates are stable.

The second step of RVNP is to minimize  $\mathcal{L}(\phi, \boldsymbol{\alpha})_V$  for  $\phi, \boldsymbol{\alpha}$ . Assuming that the likelihood function has been learnt exactly, this objective is theoretically motivated by maximising the evidence of the data. This returns error model parameters and posterior parameters that maximise the evidence lower bound.

---

### 3.3 Posterior tuning

RVNP-T, the tuned variant of RVNP, includes an extra tuning step that fixes the neural network parameters of the error model  $\alpha$ , and uses the original simulated dataset  $D$  to optimise the adjusted NPE objective

$$\mathcal{L}(\phi)_{\text{NPE}(\alpha)} := -\mathbb{E}_{p(\mathbf{x}_{\text{sim}}, \boldsymbol{\theta})} \mathbb{E}_{p_{\alpha}(\mathbf{x}_{\text{obs}} | \mathbf{x}_{\text{sim}}, \boldsymbol{\theta})} [\log q_{\phi}(\boldsymbol{\theta} | \mathbf{x}_{\text{obs}})]. \quad (14)$$

This final objective can be identified with the noisy neural posterior estimation (NNPE, Ward et al. 2022) objective and the error augmentation method suggested by Cranmer et al. (2020). However, our error model does not have to be globally fixed and has been inferred using variational inference.

### 3.4 Error modelling

Theoretically, any model can be introduced within the RVNP framework. However, we opted to only include error models that can inflate the error on the simulator model. The default error model that we adopt in RVNP is given by the Gaussian covariance matrix

$$\boldsymbol{\xi}(\boldsymbol{\theta}; \boldsymbol{\alpha}) = \text{Diag}(\text{NN}(\boldsymbol{\theta}; \boldsymbol{\alpha})) + \boldsymbol{\Lambda}, \quad (15)$$

a neural network that outputs the diagonal components of the covariance matrix and the non-diagonal components  $\boldsymbol{\Lambda}$  are globally inferred. The second model we include is a global Gaussian model

$$\boldsymbol{\xi}(\boldsymbol{\theta}; \boldsymbol{\alpha}) = \boldsymbol{\alpha}, \quad (16)$$

defined through a full rank Gaussian covariance matrix that is parametrised in terms of a Cholesky decomposition. This error model is constant across the parameter space and does not explicitly depend on  $\boldsymbol{\theta}$ .

Our method generalises very easily to include any inductive bias that we believe explains the simulation-to-reality gap. Our approach can be understood in terms of the simulator defining a population prior  $p(\boldsymbol{\theta}, \mathbf{x}_{\text{sim}}) = p_{\Psi}(\mathbf{x}_{\text{sim}} | \boldsymbol{\theta})p(\boldsymbol{\theta})$  and the error model representing the likelihood of  $\mathbf{x}_{\text{sim}}$  for the observed data.

### 3.5 Prior over the correction model parameters

In RVNP, a prior over the error model parameters  $p(\boldsymbol{\alpha})$  can be introduced to regularise the influence of the error model parameters. In our experiments, we **assume**  $\log p(\boldsymbol{\alpha}) = 0$  over the error model parameters.

## 4 Experiments and results

We test the main claim of our paper: that RVNP and its tuned variant can recover robust amortised posterior inference. In each task, we chose a fixed simulation budget of  $N_{\text{sim}} = 100,000$  and retained 10% for validation. For the three synthetic tasks, we test our methods for  $N_{\text{obs}} \in \{1, 10, 100, 1000, 10000\}$  points. For the task using real astronomical data, we test our methods for  $N_{\text{obs}} \in \{1, 10, 100, 1000\}$  due to limitations on the available data. Furthermore, we implemented sample-importance-resampling with 5000 particles and 100 samples per particle. In the experiments section, we test three variants of our algorithm

- RVNP: the standard RVNP algorithm with no final tuning step, using the error model given in Equation 15.
- RVNP-G: the standard RVNP algorithm with no final tuning step, using the global error model given in Equation 16.
- RVNP-T: the tuned version of RVNP.

For the RVNP and the RVNP-G algorithm, we evaluate the metrics with and without sample-importance-resampling. For both the variational posterior and the simulator proxy, we used neural spline flows (Durkan

et al., 2019), and the hyperparameters were kept consistent among the tasks. An overview of the architecture and training procedure for each task is described in the appendices.

**Benchmarking Algorithms.** In these tasks, we benchmark RVNP against noisy neural posterior estimation (NNPE) from Ward et al. (2022) because NNPE is a robust amortised Bayesian inference algorithm. Furthermore, NNPE exhibits similar performance relative to their robust neural posterior estimation algorithm, which is not suited to amortised inference. We do not benchmark against the unsupervised domain adaptation or consistency loss methods for amortised Bayesian inference (Elsesüller et al. 2025; Mishra et al. 2025) due to their dynamic adaptation of the embedding space. We also benchmark against standard NPE.

**Summary of Results.** We found that RVNP and RVNP-T can recover robust posterior inference in an amortised manner across a range of different tasks, including cases where a significant number of points have ID data. RVNP-T does not increase the robustness of the posterior across any task, and should be avoided unless the practitioner believes the error model has been inferred globally and wants to infer posteriors on streaming data in a fast manner. Furthermore, we found that sample-importance-resampling from the variational posterior increases the posterior performance slightly.

Our methods performed well against the benchmark algorithms except for the  $N_{\text{obs}} = 1$  case, where we find that our algorithm is always overconfident to a certain degree. This is not surprising, as RVNP is highly overparametrised without enough data to learn the error model reliably. With stronger priors on misspecification and reducing the flexibility of the error model, we could make this step more robust. However, this defeats the purpose of allowing the data to drive the error model. Furthermore, we do not attempt to address robustness in the non-amortised inference problem, but include it for completeness.

We show examples of posterior inference in the  $N_{\text{obs}} = 1000$  case for RVNP against NPE for each of the tasks for a single example in Figure 2. We argue that the success of RVNP, the interpretability of the error correction model, and the lack of misspecification-dependent hyperparameters to set, amount a significant contribution to robust amortised SBI.

#### 4.1 Metrics for assessing misspecification

We consider four metrics to assess the robustness of the inference. Let  $\theta^*$  be the true value of the parameter. Assuming that we have a labelled test set  $T = \{\theta^{*(i)}, \mathbf{x}_{\text{obs}}^{(i)}\}_{i=1}^{N_{\text{test}}}$ , we evaluate the **log posterior probability** (LPP) of the true parameter for all points in the dataset. LPP has been extensively used in SBI literature to assess performance, and is a useful metric for assessing the ability to predict the truth from observation (Papamakarios & Murray 2016; Hermans et al. 2020; Ward et al. 2022; Kelly et al. 2024; Wehenkel et al. 2025).

Given a credible level  $\gamma$ , let  $\text{HDR}_{q_\phi}(\theta | \mathbf{x}_{\text{obs}})(1 - \gamma)$  represent the  $1 - \gamma$  highest posterior density region of the posterior estimator  $q_\phi(\theta | \mathbf{x}_{\text{obs}})$ . The expected posterior coverage (EPC) at a given confidence level over a test set is given by

$$\text{EPC}(\gamma) := \mathbb{E}_{\theta^*, \mathbf{x}_{\text{obs}} \sim T} [\mathbf{1}\{\theta^* \in \text{HDR}_{q_\phi}(\theta | \mathbf{x}_{\text{obs}})(1 - \gamma)\}], \quad (17)$$

where  $\mathbf{1}$  is the indicator function. EPC is a commonly used metric to assess robustness and calibration of posterior distributions (Kelly et al., 2025), particularly when looking at single observation situations. When comparing posterior calibration across a range of amortised datasets, we compute the **average expected posterior coverage** (AEPC)

$$\alpha := \int_0^1 [\text{EPC}(\gamma) - \gamma] d\gamma, \quad (18)$$

which represents the average calibration across the test set. The AEPC metric is evaluated using the density approach of Hyndman (1996) for calculating highest posterior density intervals.

We also compute the **average expected marginal posterior coverage** (AEMPC) for each parameter  $\theta_i$ , which is common when we only obtain samples of the posterior distribution (Wehenkel et al., 2025). The AEMPC can be implemented in a more stable fashion than the posterior density approach but can oversimplify the complex regions of the posterior. It is calculated by first estimating

$$\text{EMPC}(\gamma)_i := \mathbb{E}_{\theta_i^*, \mathbf{x}_{\text{obs}} \sim T} [\mathbf{1}\{\theta_i^* \in \text{HDR}_{q_\phi}(\theta_i | \mathbf{x}_{\text{obs}})(1 - \gamma)\}]. \quad (19)$$

The AEMPC is defined as

$$\alpha(\text{marginal}) := \frac{1}{m} \sum_{i=1}^m \int_0^1 [\text{EMPC}(\gamma)_i - \gamma] d\gamma, \quad (20)$$

which is necessary for comparing the coverage of the posterior when using sample-importance-resampling, as we only retrieve the unnormalised posterior associated with sample-importance-resampling distribution. We did not wish to rely on multi-dimensional density estimation methods to evaluate the posterior coverage from samples from the joint posterior, as we found that it depended on the density estimation algorithm.

Finally, we also evaluated the normalised root mean squared error (NRMSE):

$$\text{NRMSE} = \frac{1}{N_{\text{obs}}} \sum_{j=1}^{N_{\text{obs}}} \frac{\sqrt{\frac{1}{S} \sum_{s=1}^{N_{\text{samples}}} (\theta_j^* - \theta_j^{(s)})^2}}{\text{Std}(\theta_{\text{prior}})}, \quad (21)$$

which evaluates the normalised accuracy of the posterior prediction to the truth relative to the standard deviation of the prior training samples in each dimension.

#### 4.1.1 Description of Plots

We evaluated the metrics on each task and displayed the results in Figures 3, 4, 5, and 6. The purple dashed line corresponds to NNPE, and the orange dashed line corresponds to NPE. The blue points are from RVNP with the darker blue indicating sample-importance-resampling. The green points are from RVNP-G and the darker green indicates sample-importance-resampling. The red points corresponds to the tuned variant RVNP. In Appendix A.2, we show how RVNP performs on well-specified tasks.

The top-left plot in each image shows the AEPC ( $\alpha$ ) as a function of the number of observations, with the light green hue showing the desired target region. A value of 0 in this metric indicates well-calibrated. Any values less than this implies overconfidence, and positive results imply posterior under-confidence. Under-confidence is more desirable than overconfidence. The values of NPE and NNPE are independent of the number of observations because they are not tuned dynamically. The top-right plot in each image shows the LPP as a function of the number of observations, with the error bars indicating the standard deviation. The purple hue indicates the standard deviation of LLP from NNPE, and the orange hue indicates the standard deviation of LLP from NPE. A higher value of LPP is better. The bottom-left plot in each image shows the AMEPC ( $\alpha$  marginal) as a function of the number of observations, with the light green hue showing the desired target region. Similarly to AEPC, a value of 0 in this metric indicates well-calibrated. In the bottom-right plot, we show the NRMSE as a function of the number of observations, where lower values are better.

#### 4.2 Task A: CS

We reproduce the cancer and stromal cell development benchmark task from Ward et al. (2022). The simulator models the development of cancer and stromal cells in 2D space based on the locality of a cell relative to unobserved parents. This is emulated conditional on three Poisson rate parameters  $\theta = (\lambda_c, \lambda_p, \lambda_d)$ . The total number of cells  $N^c$ , number of unobserved parents  $N^p$ , and the number of daughter cells for each parent  $N_i^d$  are sampled as  $N^c \sim \text{Poisson}(\lambda_c)$ ,  $N^p \sim \text{Poisson}(\lambda_p)$ , and  $N_i^d \sim \text{Poisson}(\lambda_d)$  for  $i = 1, \dots, N^p$ . Cell locations  $\{c_i\}_{i=1}^{N^c}$  and disease origin points  $\{p_i\}_{i=1}^{N^p}$  were sampled uniformly across the 2D domain using homogeneous spatial point processes. For each origin point  $p_i$ ,  $r_i$  is the Euclidean distance to its  $N_i^d$ -th nearest cell. Cells falling within or on the boundary of this radius from  $p_i$  are designated as cancerous. Distance-based summary measures were estimated by randomly sampling 50 stromal cells. The summary statistics are as follows: N Cancer and N Stromal, the number of cancer and stromal cells, respectively; and (Mean Min Dist) and (Max Min Dist), the mean and maximum distance from the stromal cells to their nearest cancer cell, respectively. The Numba just-in-time implementation of this task was taken directly from the data products of Ward et al. (2022).

**Misspecification.** The misspecification in the observed data is introduced by removing cells in the core regions of tumours, which mimics necrosis.

**Results.** We show the results for the CS task in Figure 3 and provide an example posterior of RVNP with  $N_{\text{obs}} = 1000$  in Figure 2. We display the simulated observations together with observed points in Figure 16. In this task, the misspecification of removing cells in the core regions that mimics necrosis primarily impacts the number of cancer cells summary statistics. In Figure 8, we show the evaluation of RVNP on a well-specified version of the CS task. In Figure 12, we show the final two dimensions of the RVNP ( $N_{\text{obs}} = 1000$ ) covariance matrix eigenvalues evaluated at different points of the training data.

All versions of our algorithm can recover robust posterior inference after the  $N_{\text{obs}} = 10$  point in the CS task, performing better than NNPE and NPE. However, NNPE still performs relatively well, as the misspecification can be described by inflating the covariance along two specific axes. Both the global and the neural error covariance matrix represent a constant covariance matrix that points in a given direction that best describes the misspecification, which offers a form of model criticism for this problem. Our methods have better posterior coverage than NNPE and NPE, while at the same time achieving high log-probability and samples that are closer to the truth. Furthermore, they do not rely on any parameters that control the influence of the misspecification on the posterior.

### 4.3 Task B: SIR

We include the misspecified susceptible-infected-recovered (SIR) task from Ward et al. (2022), which takes the stochastic model of epidemic spread modelled conditional on  $\theta = (\beta, \gamma)$ , the time-varying infection rate and the recovery rate, respectively. The SIR model emulates ideal disease transmission dynamics from the susceptible ( $s$ ), infected ( $i$ ), and recovered ( $r$ ) parameters as

$$\frac{ds}{dt} = -\beta si, \quad \frac{di}{dt} = \beta si - \gamma i, \quad \frac{dr}{dt} = \gamma i. \quad (22)$$

Ward et al. (2022) employs a stochastic extension by using time-dependent transmission dynamics through a variable infection rate  $\tilde{\beta}_t$ , accounting for external factors such as policy interventions or pathogen mutations. This stochastic process is characterised using the basic reproduction number  $R_{0t} = \frac{\tilde{\beta}_t}{\gamma}$ , which follows the mean-reverting stochastic differential equation:

$$dR_{0t} = \eta \left( \frac{\beta}{\gamma} - R_{0t} \right) dt + \sigma R_{0t} dW_t, \quad (23)$$

where  $\eta$  controls the mean reversion strength of  $R_{0t}$  toward the equilibrium value  $\frac{\beta}{\gamma}$ ,  $\sigma$  represents the volatility parameter, and  $W_t$  denotes standard Brownian motion.  $\eta = 0.05$  and  $\sigma = 0.05$  are fixed and the goal is to infer the parameters  $\beta$  and  $\gamma$ . The Julia code to sample from this process was taken directly from the data products of Ward et al. (2022). The summary statistics produced in this task are the mean, median and maximum number of infections, the day of the maximum number of infections, and the day at which half of the total number of infections was reached, and the mean autocorrelation of infections with lag 1.

**Misspecification** To introduce misspecification in the observations, a small reporting delay is adopted where weekend infection counts are reduced by 5% and are added to the Monday count.

**Results.** This misspecification in this task only has a significant impact on the autocorrelation summary statistic. We show the results for the SIR task in Figure 4 and provide an example of the posterior distribution ( $N_{\text{obs}} = 1000$ ) in Figure 2. We display the simulated observations together with the observed points in Figure 17. In Figure 9, we show the evaluation of RVNP on a well-specified version of the SIR task. In Figure 13, we plot the final two dimensions of the RVNP ( $N_{\text{obs}} = 1000$ ) covariance matrix eigenvalues evaluated at different points of the training data.

In this task, the misspecification appears extremely OOD along the axis of the autocorrelation statistic. All versions of our algorithm can recover robust posterior inference after the  $N_{\text{obs}} = 10$  point, and they perform better than NNPE and NPE in this task. However, NNPE still performs well, as the misspecification can

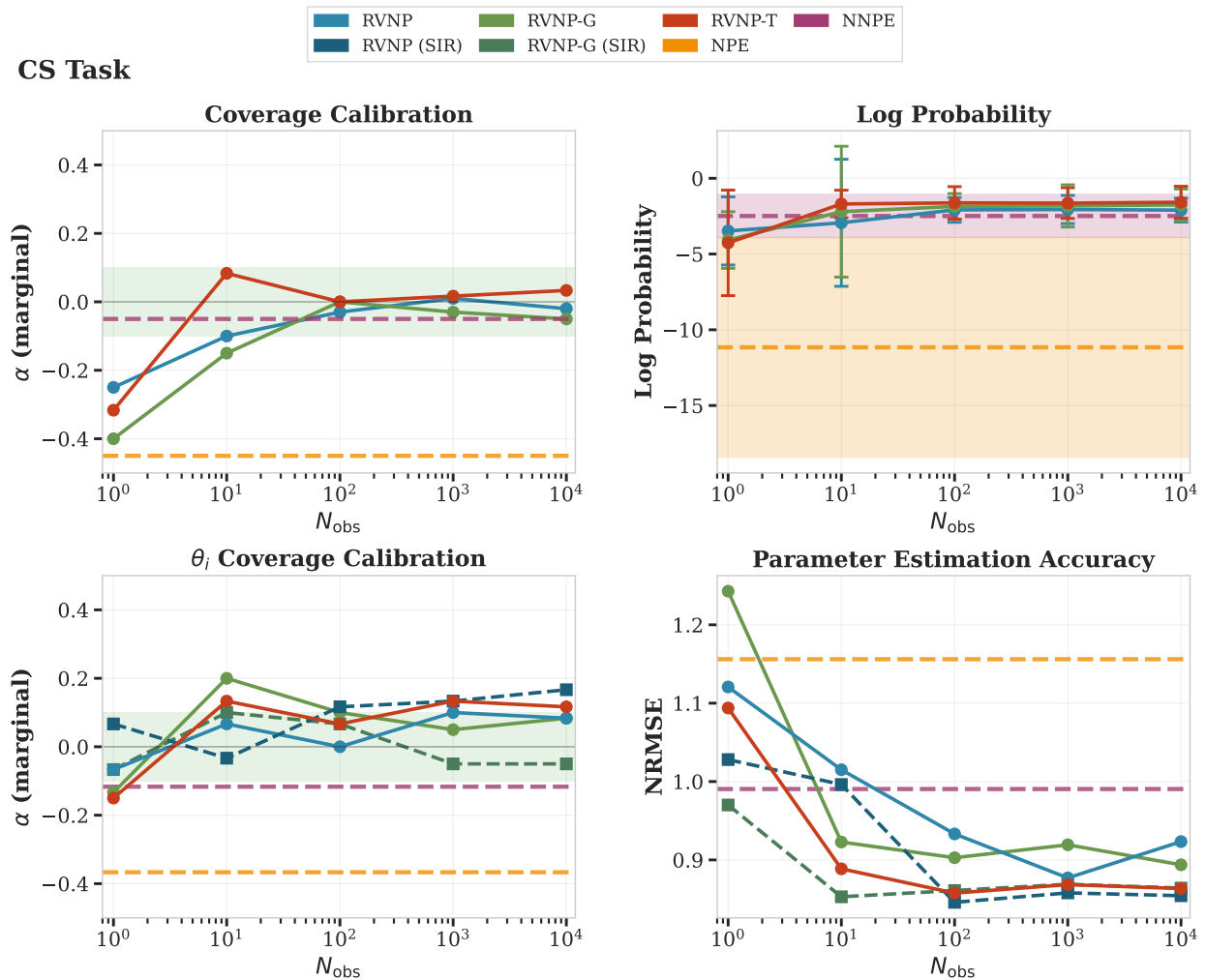


Figure 3: Results for the CS task. We conclude that RVNP and its variants can recover robust posterior inference in amortised simulation-based inference. The hue in the middle plots indicates the error bar on the NPE and NNPE algorithms. For  $\alpha$  nearest to 0 is best, with positive values representing underconfidence and negative values representing overconfidence. For the log-probability, higher values are better. For NRMSE, lower values are better. (SIR) indicates sample-importance-resampling.

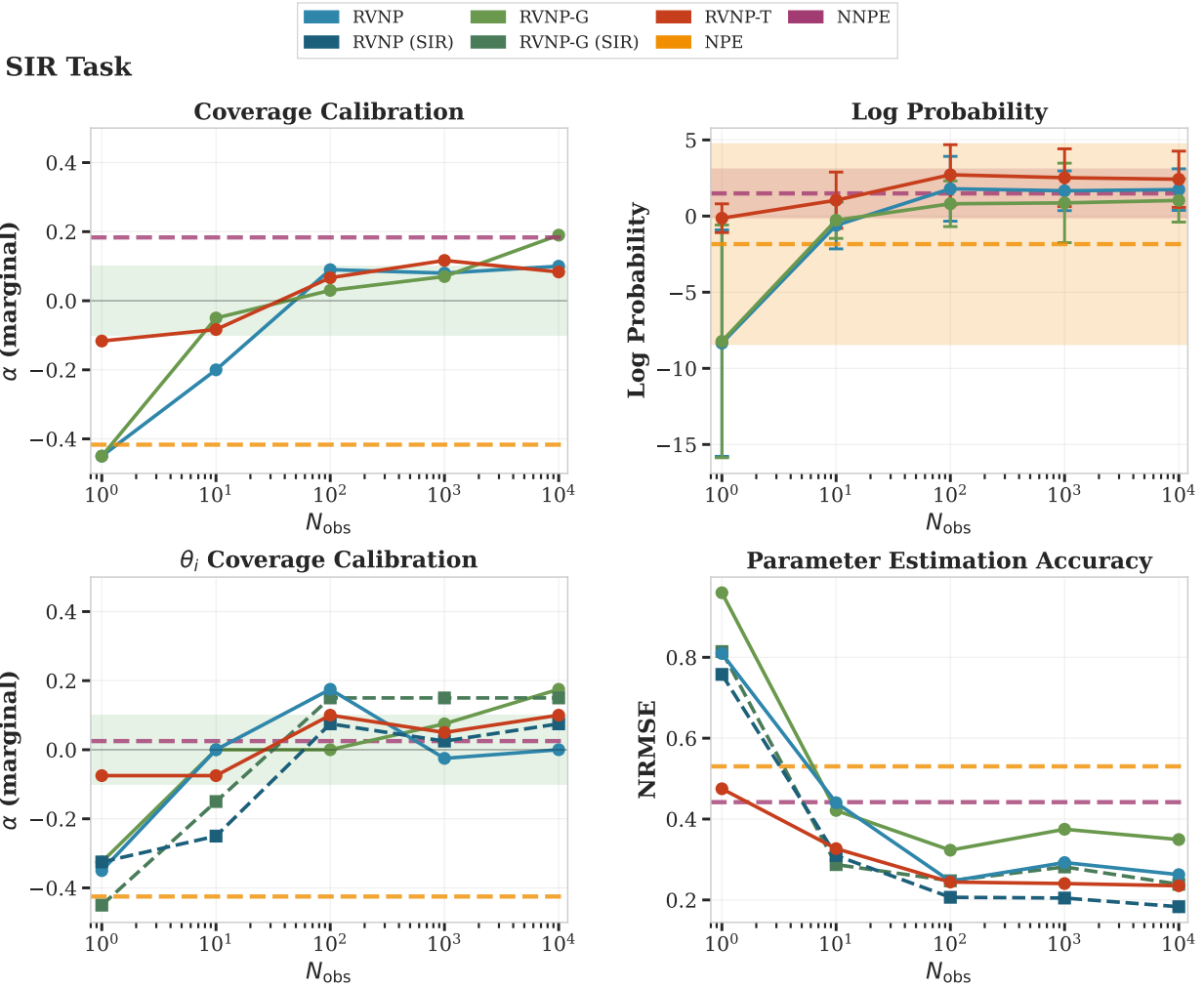


Figure 4: Results for the SIR task. We conclude that RVNP and its variants can recover robust posterior inference in amortised simulation-based inference. The hue in the middle plots indicates the error bar on the NPE and NNPE algorithms. For  $\alpha$  nearest to 0 is best, with positive values representing underconfidence and negative values representing overconfidence. For the log-probability, higher values are better. For NRMSE, lower values are better. (SIR) indicates sample-importance-resampling, not to be confused with the name of the task.

be described by inflating the covariance along the final axis. NPE performs very poorly in this task, due to the extreme misspecification along the final axis.

Our methods have better posterior coverage than NNPE and NPE, while at the same time achieving high log-probability, and samples that are closer to the truth. Furthermore, the global and neural error covariance matrix learn that the covariance inflates along the final axis. However, the neural error model outperforms the global error model, as the degree of misspecification along that axis depends on  $\theta$ . The effect of this is that both the log-probability and the NRMSE are better for RVNP than the global version, as the global version scales up the covariance to account for this misspecification everywhere.

#### 4.4 Task C: Pendulum Task

We describe a stochastic pendulum simulator that, given  $\theta := [\omega_0, A]$ , samples the horizontal position of a frictionless pendulum at 200 time points evenly sampled every 0.05 seconds  $\mathbf{x}_{\text{sim}} = (f(t_0), \dots, f(t_{200}))$  where  $f(t) = A \cos(\omega_0 t + \phi)$  for  $\phi \sim U(-\pi, \pi)$ . In this task,  $\omega_0$  and  $A$  denote the fundamental frequency and amplitude, respectively, of the frictionless pendulum.  $\phi$  is a stochastic phase shift. This task was inspired by the task from Wehenkel et al. (2025). However, it differs significantly and was adjusted to test our claim that increasing the number of posterior observations will better constrain the parameters.

**Misspecification** We synthesise a time calibration error in the instrumentation that causes the instrument to take 200 measurements every 0.075 seconds instead of the simulated 0.05 seconds. There is a significant probability that the misspecified point will appear ID due to the form of the misspecification.

**Neural Statistic Estimation** In this example, each of the data points is a single observation. The neural statistic estimator is an embedding of the full pendulum time series into a lower-dimensional representation of the data. Following Chen et al. (2021), we use the Shannon-Jensen InfoMax objective (Hjelm et al., 2019) to target sufficient neural statistics,  $\iota_{\omega}$ , to encode the high-dimensional data. This objective function maximises the mutual information between  $\mathbf{x}_{\text{sim}}$  and  $\theta$  using a discriminator network. We give an overview of the chosen architecture in the appendices.

**Results.** We show the results for the Pendulum task in Figure 5. In Figure 2, we display an example of the posterior distribution in the  $N_{\text{obs}} = 1000$  case. We show the simulated observations together with the observed points in Figure 18. In Figure 10, we evaluate RVNP on a well-specified version of the Pendulum task. In Figure 14, we plot the final two dimensions of the RVNP ( $N_{\text{obs}} = 1000$ ) covariance matrix eigenvalues evaluated at different points of the training data.

In this task, the misspecification appears more complex geometrically. Moreover, due to the nature of the misspecification, most of the points will appear ID relative to the simulated training points. All versions of our algorithm can recover more robust posterior inference beginning after the  $N_{\text{obs}} = 10$  point than the NNPE and NPE. NNPE struggles significantly, most likely due to the spike-and-slab error model being unable to account for such a complex misspecification. However, RVNP and RVNP-G recover robust posterior inference for this task. In particular, RVNP is well calibrated after the  $N_{\text{obs}} = 100$  point and recovers robust posterior inference across a broad range in parameter space. Furthermore, RVNP is reasonably well calibrated. Due to the complexity of the error model, the tuned variant, RVNP-T, does not see the same degree of performance increase. However, it does perform better than both NPE and NNPE. NPE performs very poorly in the pendulum task. Both covariance models have their largest eigenvector pointing in the direction of changing fundamental frequency, as expected.

#### 4.5 Task D: Spectra Task - Real Gaia BP/RP Data

The third data release of the European Space Agency’s Gaia telescope (Gaia Collaboration, 2016) contain over 220 million flux-calibrated, low-resolution, optical stellar spectra. These spectra are measured by two instruments, the “Blue Photometer” (BP, 330-680 nm coverage in wavelength) and the “Red Photometer” (RP, 640-1050 nm). The processed and calibrated (De Angeli, F. et al. 2023; Montegriffo, P. et al. 2023) BP/RP (XP) spectra from Gaia DR3 are low-resolution, contaminated spectra which have multiple difficult systematics to overcome (Huang et al., 2024). However, the XP spectra are expected to contain significant information about different stellar parameters (Witten et al., 2022) and robust posterior inference using stellar

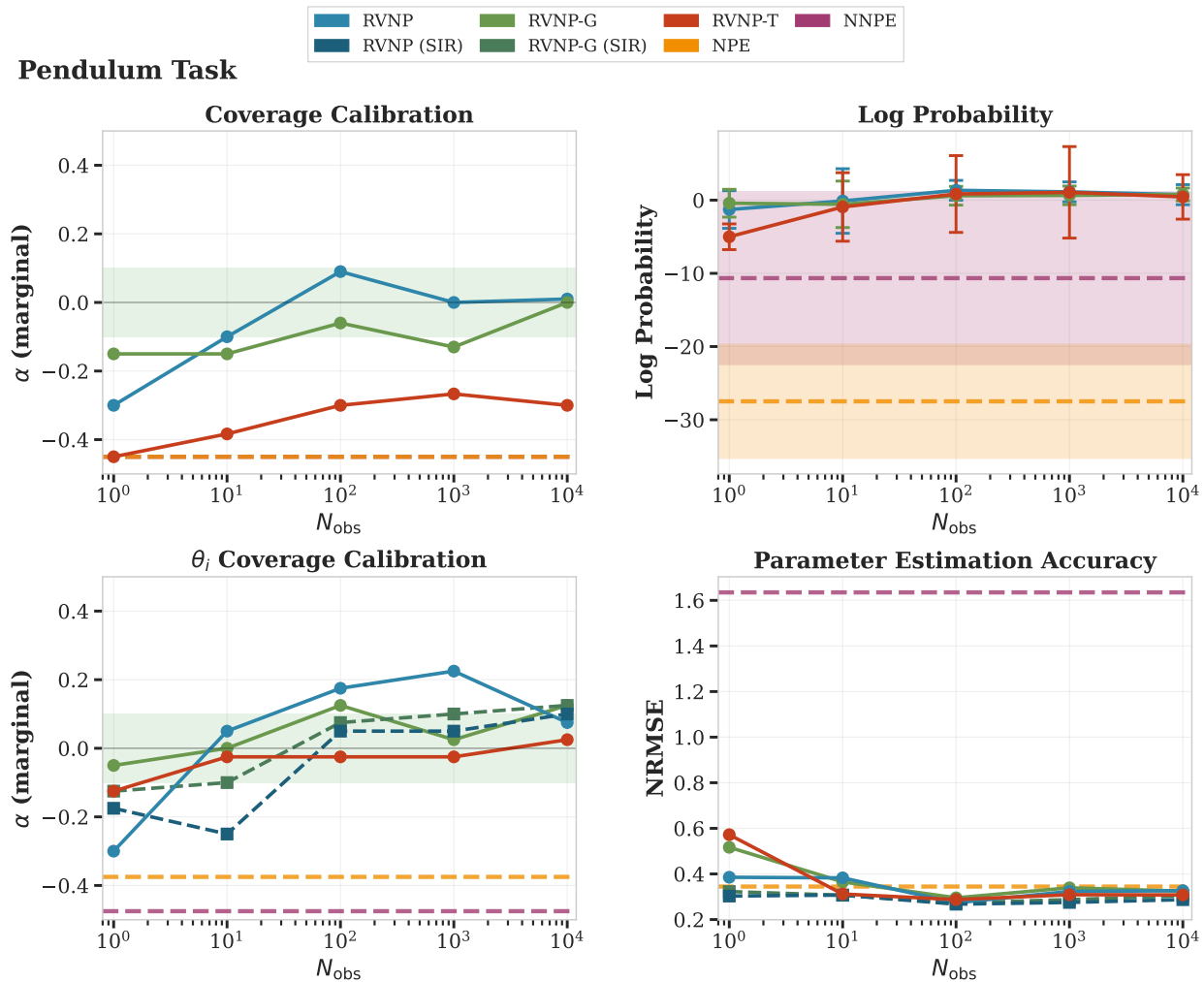


Figure 5: Results for the Pendulum task. We conclude that RVNP and its variants can recover robust posterior inference in amortised simulation-based inference. The hue in the middle plots indicates the error bar on the NPE and NNPE algorithms. For  $\alpha$  nearest to 0 is best, with positive values representing underconfidence and negative values representing overconfidence. For the log-probability, higher values are better. For NRMSE, lower values are better. (SIR) indicates sample-importance-resampling

---

evolution simulators conditional on the Gaia XP spectra would provide an efficient method for understanding the Milky Way.

**Simulator** We use the MIST Choi et al. (2016) stellar evolution models to generate stellar parameters compatible with high Galactic latitudes (a region where observable contaminants are low) and map each of the effective temperature, log-surface gravity, and metallicity to a medium-resolution synthetic Castelli & Kurucz (2004) model spectrum. This defines a stochastic simulator mapping  $\theta = (T_{\text{eff}}, \log g, [\text{Fe}/\text{H}])$  to  $\mathbf{x}_{\text{sim}}$ . We restrict the spectra in their native resolution between 330-1050 nm to define a 301 dimensional vector which overlaps with the Gaia XP spectra wavelength, but at a significantly different resolution.

**Embedding** We pre-train an NSE estimator using the same method as described in the pendulum task.

**Misspecification:** We can view the problem of inferring stellar parameters using real Gaia XP spectra and synthetic stellar evolution models as a misspecification problem. The Gaia XP spectra are expected to have two significant differences from the synthetic simulation model. Firstly, the XP spectra are lower resolution than the synthetic spectra and, therefore, contain less information. Secondly, there are inherent systematic errors in the processing of the XP spectra and in the stellar evolution modelling that causes a simulation gap even if we knew the spectroscopic parameters exactly. For the real dataset, we target high Galactic latitudes due to the minimal impact of dust extinction and other contaminants (O’Callaghan et al., 2024). We select all stars with absolute Galactic latitude  $|b| > 80^\circ$  that have valid LAMOST (Wang, 2022) spectroscopically determined stellar parameters. These spectroscopically determined stellar parameters will act as ground truth for our experiment, but we should note that they have their own errors arising from the spectroscopic determination. Furthermore, we select all Gaia recommended quality cuts and choose stars with confident distance estimates between 300 and 700 pc. This leaves us with a dataset of size  $N_{\text{obs}} = 1053$ .

**Results.** We show the results for the Spectra task in Figure 6 and provide an example posterior in the  $N_{\text{obs}} = 1000$  case in Figure 2. We display the simulated observations together with the observed points in Figure 19. In Figure 11, we evaluate RVNP on a well-specified version of the Spectra task. In Figure 15, we plot the final two dimensions of the RVNP ( $N_{\text{obs}} = 1000$ ) covariance matrix eigenvalues evaluated at different points of the training data.

In the spectra task, the misspecification is geometrically very complex. This arises from using a neural statistic embedding and from the complexity of stellar evolution models. Many of the points appear ID relative to the simulated points in this task. We naively applied the neural statistic, so that the neural statistic knows nothing about the structure of the Gaia XP spectra, including instrument response and measurement error. The RVNP and RVNP global algorithms can recover robust posterior inference beginning after the  $N_{\text{obs}} = 10$  point. We find that both of these algorithms perform better than NNPE and NPE. However, RVNP-T collapses to the NPE posterior after tuning. NNPE struggles significantly, most likely due to the spike-and-slab error model being unable to account for such a complex misspecification. RVNP-G is very well calibrated after the  $N_{\text{obs}} = 100$  point and recovers robust posterior inference across a broad range of parameter space. Furthermore, RVNP is reasonably well calibrated, particularly when considering the marginal calibration metric. NPE performs very poorly in the pendulum task in terms of calibration and log-probability, but its sampled points are close to the truth, reflecting an extreme overconfidence.

Investigating the covariance matrix of the error models helps us to understand why the global variant performs better. In certain points of parameter space where the covariance matrix has not observed data, the posterior collapses to the NPE estimate, and near these points the inference is less reliable. The covariance matrix provides useful model criticism by considering the error as a function of  $\theta$ . We find that we cannot recover the metallicity estimate reliably. This is not surprising because the resolution of the synthetic spectra is higher than that of the observed data, and the metallicity will appear as strong local features in the spectra. These features are not present in the Gaia BP/RP spectra. Domain adaptation approaches that can account for these difference may be desirable in this context.

## 5 Related work

**Misspecification in SBI** Model misspecification is understood in likelihood-based methods (Davison 2003, pages 147–148); however, a systematic theory of likelihood-free methods is lacking. Misspecification in SBI

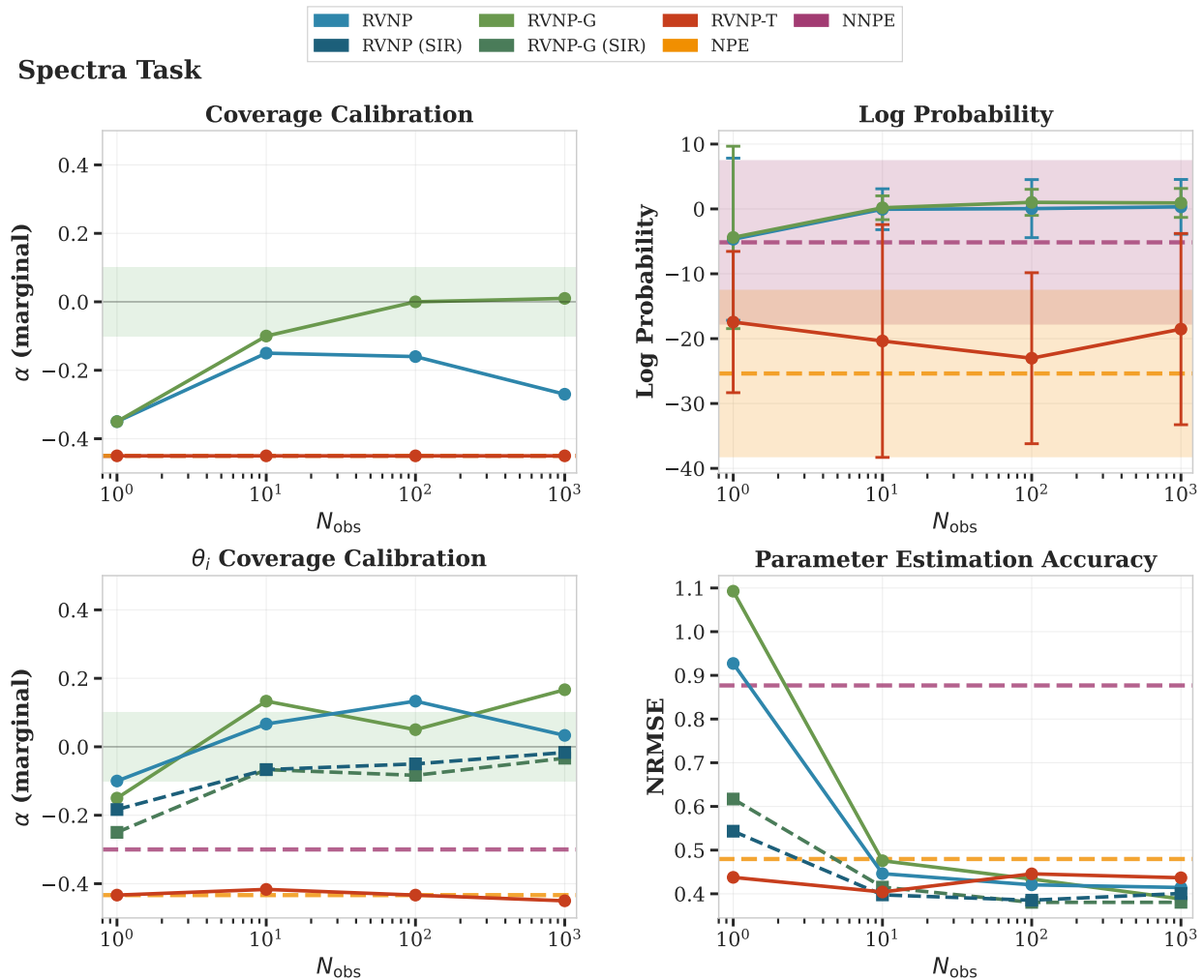


Figure 6: Results for the Spectra task. We conclude that RVNP and its variants can recover robust posterior inference in amortised simulation-based inference. The hue in the middle plots indicates the error bar on the NPE and NNPE algorithms. For  $\alpha$  nearest to 0 is best, with positive values representing underconfidence and negative values representing overconfidence. For the log-probability, higher values are better. For NRMSE, lower values are better. (SIR) indicates sample-importance-resampling.

---

has been studied in the context of ABC (Frazier et al. 2020; Bharti et al. 2022; Fujisawa et al. 2021), BSL (Frazier et al., 2024), generalized Bayesian inference (Dellaporta et al., 2022), and neural conditional density estimation (Ward et al. 2022; Kelly et al. 2024; Huang et al. 2023; Elsemüller et al. 2025; Mishra et al. 2025; Schmitt et al. 2024; Wehenkel et al. 2025). In this paper, we focused on neural-based methods, where empirically it has been shown that SBI struggles under model misspecification (Cannon et al. 2022; Schmitt et al. 2024). Robust posterior recovery under model misspecification is essential for the success of SBI, and different methods have emerged to mitigate against it. Kelly et al. (2025) identifies three main strategies currently used to account for model misspecification in SBI: robust summary statistics, generalised Bayesian inference, and error modelling and adjustment parameters. Most of the early solutions in robust SBI were intended for a single data set (Ward et al. 2022; Kelly et al. 2024; Huang et al. 2023).

**Robust amortised SBI** Recently, robust amortised neural SBI has been addressed using optimal transport for domain shifts when a calibration set exists (Wehenkel et al., 2025), using unsupervised domain adaptation (Elsemüller et al., 2025), and consistency losses regularisation (Mishra et al., 2025). Moreover, Glöckler et al. (2023) proposes regularisation techniques to increase the robustness of the learnt posterior against adversarial attacks. Of these methods, only the consistency loss method targets both the likelihood and the posterior. The noisy neural posterior estimation from Ward et al. (2022) can also be viewed as an amortised SBI method, where a pre-defined error model is used during training to corrupt the simulations.

**Variational methods in SBI** Variational methods have been used in multiple capacities to date. Wqvist et al. (2021) introduced Sequential Neural Posterior and Likelihood Approximation, which proposes using variational inference (VI) to speed up the inference of likelihood-based methods, similar to the likelihood-based Bayesian approach to VI. Glöckler et al. (2022) introduces a framework that uses VI for simulation-based inference by using a pre-trained likelihood (or likelihood-ratio) and learn the posterior using VI, then refining the posterior using sampling importance resampling (Rubin, 1987). Nautiyal et al. (2024) introduces a generative modelling approach based on the variational inference framework and learns an encoder-decoder model in terms of latent variables. They introduce a latent variable that can account for complex structures and dependencies in the simulator model. Simons et al. (2022) propose a simulation-based inference algorithm that iteratively updates particles to more match the posterior in a variational likelihood-free gradient descent manner. Moreover, Dax et al. (2023) use a trained NPE for importance-sampling in a likelihood-based manner.

## 6 Discussion and limitations

In this paper, we introduced RVNP(-T), a robust amortised Bayesian inference method for simulation-based inference that jointly infers the simulation-to-reality gap and the amortised posterior using an importance-weighted autoencoder framework. RVNP is the first example of using variational inference for robust simulation-based inference, and was inspired by robust SBI approaches for synthetic likelihood (Frazier & Drovandi, 2021), neural posterior estimation (Ward et al., 2022), and sequential neural likelihood estimation (Kelly et al., 2024). We argue that RVNP’s novelty and its ability to recover robust amortized posterior inference without setting misspecification-related tuning parameters constitutes an important step toward reliable posterior inference in amortised SBI. Previous work’s reliance on setting a hyperparameter or misspecification prior to control the influence of the misspecification on the posterior inference is undesirable, and as more data are observed we will have a better understanding of the simulation-to-reality gap, which should inform the inference without strong assumptions on the degree of misspecification. Moreover, RVNP is reliable in the well-specified case.

Our work is not without limitations, and in what follows we discuss the scope of RVNP, how it relates to previous error modelling approaches, the use of neural statistic embeddings, and the implications of using variational inference to infer the posterior.

### 6.1 Error Modelling

Including an error model is an assumption about how to model the true data-generative process (DGP) under the assumption that observed data appears corrupted relative to the model simulations. In most real-world

problems, the exact corruption is unknown and there are infinitely many distributions and assumptions that can bridge the simulation-to-reality gap. In this paper, we imposed a strong inductive bias on the distribution that bridges it, so that the error model accounts for the corruption by inflating the error on the synthetic DGP. This choice is a neural adaptation of the covariance inflation from Frazier & Drovandi (2021). The simulation-to-reality gap should inform our error model as we observed more data from the true DGP, particularly if the misspecification is a global phenomenon (Figure 1). By jointly inferring the posterior and the error model, we can allow the error model parameters to be inferred directly from the data without having tunable parameters that dictate the strength of the misspecification (for example, a shrinkage prior over the adjustment parameters (Kelly et al., 2024) or the misspecification regularisation in unsupervised domain adaptation (Huang et al., 2023)).

Similarly to the spike-and-slab error model introduced by Ward et al. (2022), the error models introduced in this paper allows us to have a form of *model criticism*. We argue that without prior knowledge about the misspecification, inflating the error of the output of the simulator is the most sensible approach, as it is interpretable and allows for a level of trust in the inference procedure. The spike-and-slab model invokes a similar assumption: that the true corruption model is unknown and the misspecification encourages the posterior to forget certain summary statistics if they lie OOD. This relies on the misspecification appearing along individual axes in summary-statistic space, which is unrealistic in many situations because misspecification has no guarantee of appearing along given axes. Furthermore, the success of the spike-and-slab error model is subject to hyperparameter choices that dictate the strength of misspecification. We found that in the pendulum and the spectra task NNPE performed poorly for these reasons.

The parameter adjustment method of Kelly et al. (2024) can be thought of as an error model  $p_{\alpha}(\mathbf{x}_{\text{obs}}|\mathbf{x}_{\text{sim}}) = \delta(\mathbf{x}_{\text{obs}} - \mathbf{x}_{\text{sim}} - \alpha)$  after integrating with respect to  $\mathbf{x}_{\text{sim}}$ , where  $\alpha$  are the linear adjustment parameters. This approach will move the observed point in summary-statistic space to a region of high probability with respect to the simulated samples. On a point-by-point basis, there are infinitely many solutions to this problem, and there is no guarantee of where an OOD point should be mapped back to in the original sample without extra information on the misspecification, such as a calibration set. Moreover, Kelly et al. (2024) state that the ability to recover robust posterior inference in their benchmark tasks depends on the hyperparameters that control the strength of the misspecification, which is difficult to set in practice.

The flexibility of the RVNP error model also gives rise to certain limitations. In RVNP, we are required to choose an error model architecture together with network hyperparameters. Although the neural-network parametrised error model performs more favourably than the global covariance in most of the tasks, there are two issues which can arise from its implementation. Firstly, we fixed the architecture capacity, implying that the neural-network covariance matrix is massively over-parametrised in the  $N_{\text{obs}} = 1$  and 10 cases. Secondly, as highlighted in the spectra task, the highly nonlinear bridging of the simulation-to-reality through covariance inflation gap may not be suitable if many of the points lie within distribution in a manner that cannot be distinguished by  $\theta$ . In the spectra task, significant subsets of  $\Theta$  are mapped to observed points in a manner that the covariance matrix collapsed to a delta on the subset. We believe that a reliable calibration set that covers such subsets can address these collapses. The impact of a complex bridging of the simulation-to-reality gap has also been witnessed in unsupervised domain adaptation (Elsemler et al., 2025).

Introducing an error model inherently adds noise into the forward model. We found that the lowest the covariance would decrease to in the well-specified tasks amounted to a standard deviation of 0.01 on the Gaussian uncertainty in each direction. While small, if the simulator is very sensitive to changes in the underlying parameters this could be consequential. Hermans et al. (2022) observe that SBI methods tend to produce overconfident posterior approximations in general, and perhaps introducing an error model in this situation is less problematic.

## 6.2 Choice of summary statistics

In this paper, we used summary statistics that are hand-crafted and those that are inferred using a neural statistic estimator (NSE).

---

Interpretable, hand-crafted summary statistics, or preparing the data into a manageable form with physically motivated units is often highly desirable (Kelly et al., 2025). In the context of misspecification, hand-crafted summary statistics allow RVNP to be used when inferring the misspecification for the purpose of model criticism, providing an understanding of the discrepancies between the simulator model and the data to the practitioner. Often, scientific discoveries are made in physical units by fitting for the discrepancy between the model and the observed data. For example, in astronomy dust extinction is inferred by comparing the global misspecification between the simulator and the observed spectral data. In RVNP, we return both the posterior and the forward model, allowing us to inspect and criticise the model, but also recover fast and robust posterior inference that can readily be applied to large datasets.

Adopting a neural statistic estimator (NSE) to embed the data into a low-dimensional representation can be highly valuable in SBI if the data is complex and high-dimensional (Deistler et al., 2025). As RVNP is an extension of neural likelihood estimation (NLE) we cannot jointly learn the NSE and the likelihood proxy in an end-to-end fashion (Brehmer & Cranmer, 2020). A downside of this is that we have to specify separate hyperparameters for the optimiser when inferring the NSE. However, staged training allows us to choose objectives that guarantee global sufficiency (Chen et al., 2021), which may be highly desirable for amortised Bayesian inference. As RVNP pre-trains the NSE, we can use the InfoMax objective (Hjelm et al., 2019) and benefit from its theoretical guarantees of global sufficiency. A staged training allows us to decouple the inference from learning the NSE, and can help the Bayesian workflow if the main computational difficulty is in dealing with the high-dimensional data once simulated. This is true particularly for amortised learning where global sufficient statistics are needed and an up-front simulation budget is defined. Non-amortised methods train in rounds, often making end-to-end methods more appealing.

When learning the NSE and the posterior in an end-to-end fashion, a form of domain adaptation is necessary to account for misspecification. While this will help against the observed data having a very poor representation under the NSE, there is an inherent trade-off between learning the posterior and accounting for the misspecification in a manner that depends on a user-defined hyperparameter. Although RVNP requires more tunable hyperparameters as a result of the variational inference (and the InfoMax objective, if adopted), it requires no parameters that dictate the strength of the misspecification.

Similarly to error modelling, complex domain adaptation in a nonlinear fashion may have infinitely many solutions that can account for the simulation-to-reality gap in a manner that is highly uninterpretable, and offers very little model criticism. A separate body of work should discuss error modelling using calibration set, and compare with the results of Wehenkel et al. (2025).

### 6.3 Prior misspecification

Prior misspecification was not explicitly addressed within the RVNP tasks. Assuming that the neural likelihood proxy is learnt exactly, RVNP should have the same limitations as likelihood-based prior misspecification if the support of the adjusted prior is a subset of the support of the original prior used to train the likelihood. In reality, the ability to train the likelihood is influenced by the prior over  $\theta$ , and it may struggle to learn the distribution in regions where there are a low density of points.

In the experiments, we chose relatively uninformed priors. However, we stress that the pendulum task benefits from the uniform bounds in  $\theta$  defined to generate the simulator samples. In the pendulum task, the points appear OOD under the misspecification because its effect makes the points *appear* as if they have a higher fundamental frequency relative to the summary statistics. However, the information about the misspecification is only available to us because we assume that the prior is well-specified and that there is an upper bound to the fundamental frequency. With expert knowledge this is not an unreasonable assumption. However, we would lose the robustness of the inference if we assumed a wider prior on the fundamental frequency, causing the synthetic DGP to cover the observed data points. Therefore, there is a trade-off between extending the prior to higher fundamental frequencies and robustness.

We note that in the Spectra task we defined a wide, poorly-adopted prior relative to the observed data, which occurred unintentionally due to the selection effects of the real data. However, this did not cause any issues. There are, however, hard boundaries along a certain direction due to the sharp cut off expected from observed metallicities.

---

## 6.4 Variational Inference and sample-importance-resampling

RVNP builds on variational methods for solving the inverse problem under a learnt likelihood in SBI (Glöckler et al., 2022), and relies on a conditional neural density estimator to approximate the likelihood from a fixed budget of simulations from the simulator model. In this sense, RVNP extends NLE by accounting for misspecification using an error model. We invoke variational inference to overcome the computational expense of using Hamiltonian Monte Carlo Neal (2011) or other Markov Chain methods to jointly infer the parameters of interest and the parameters of the error model. The sharing of the parameters over a large model makes the inference highly dependent on the gradients, and struggles to converge even for a diagonal Gaussian covariance error model. Furthermore, variational methods allow us to use more expressive models for the error model distribution.

NLE methods require more hyperparameter tuning and model choice by adopting the variational inference posterior, which also comes at an increased computational expense (Deistler et al., 2025). However, if the amortised likelihood has been trained well, variational methods with sample-importance-resampling can compete with the accuracy of NPE (Glöckler et al., 2022). Importantly for the misspecification problem, while we increase the number of tunable parameters and architecture choices for the inference step, we do not adopt hyperparameters that control the strength of the misspecification. In this situation, the difficulty arises from the *inference step* as opposed to accounting for the misspecification. We argue that this is sensible for misspecification.

In general, we find that sample-importance-resampling is important for making the inference more robust. In particular, it is useful for "cleaning samples" that the posterior has generated which are not compatible with the prior distribution or the likelihood. We present an example of this in Figure 7.

### Author Contributions

The programming and the writing of the paper was carried out by MOC.

### Acknowledgments

MOC is supported by the Gianna Angelopoulos Programme for Science, Technology and Innovation (GAP-STI) through the Science and Technology Facilities Council (STFC) studentship for astronomy. GG acknowledges support from The Leverhulme Trust, through Emeritus Fellowship 2025-007. KSM is supported by the European Union's Horizon 2020 research and innovation programme under European Research Council Grant Agreement No 101002652 (BayeSN) and Marie Skłodowska-Curie Grant Agreement No 873089 (ASTROSTAT-II).

### References

- Mark A Beaumont, Wenyang Zhang, and David J Balding. Approximate bayesian computation in population genetics. *Genetics*, 162(4):2025–2035, 12 2002. ISSN 1943-2631. doi: 10.1093/genetics/162.4.2025. URL <https://doi.org/10.1093/genetics/162.4.2025>.
- Ayush Bharti, Louis Filstroff, and Samuel Kaski. Approximate bayesian computation with domain expert in the loop. In *International Conference on Machine Learning*, pp. 1893–1905. PMLR, 2022.
- Michael GB Blum, Maria Antonieta Nunes, Dennis Prangle, and Scott A Sisson. A comparative review of dimension reduction methods in approximate bayesian computation. 2013.
- Johann Brehmer and Kyle Cranmer. Flows for simultaneous manifold learning and density estimation. *Advances in neural information processing systems*, 33:442–453, 2020.
- Yuri Burda, Roger Grosse, and Ruslan Salakhutdinov. Importance weighted autoencoders. *arXiv preprint arXiv:1509.00519*, 2015.
- Patrick Cannon, Daniel Ward, and Sebastian M Schmon. Investigating the impact of model misspecification in neural simulation-based inference. *arXiv preprint arXiv:2209.01845*, 2022.

- 
- F. Castelli and R. L. Kurucz. New grids of atlas9 model atmospheres, 2004.
- Yanzhi Chen, Dinghuai Zhang, Michael U. Gutmann, Aaron Courville, and Zhanxing Zhu. Neural approximate sufficient statistics for implicit models. In *International Conference on Learning Representations*, 2021. URL <https://openreview.net/forum?id=SRDuJssQud>.
- Jieun Choi, Aaron Dotter, Charlie Conroy, Matteo Cantiello, Bill Paxton, and Benjamin D. Johnson. Mesa Isochrones and Stellar Tracks (MIST). I. Solar-scaled Models. *apj*, 823(2):102, June 2016. doi: 10.3847/0004-637X/823/2/102.
- Kyle Cranmer, Juan Pavez, and Gilles Louppe. Approximating likelihood ratios with calibrated discriminative classifiers, 2016. URL <https://arxiv.org/abs/1506.02169>.
- Kyle Cranmer, Johann Brehmer, and Gilles Louppe. The frontier of simulation-based inference. *Proceedings of the National Academy of Sciences*, 117(48):30055–30062, May 2020. ISSN 1091-6490. doi: 10.1073/pnas.1912789117. URL <http://dx.doi.org/10.1073/pnas.1912789117>.
- Chris Cremer, Quaid Morris, and David Duvenaud. Reinterpreting importance-weighted autoencoders, 2017. URL <https://arxiv.org/abs/1704.02916>.
- Anthony Christopher Davison. *Statistical models*, volume 11. Cambridge university press, 2003.
- Maximilian Dax, Stephen R Green, Jonathan Gair, Michael Pürer, Jonas Wildberger, Jakob H Macke, Alessandra Buonanno, and Bernhard Schölkopf. Neural importance sampling for rapid and reliable gravitational-wave inference. *Physical review letters*, 130(17):171403, 2023.
- De Angeli, F., Weiler, M., Montegriffo, P., Evans, D. W., Riello, M., Andrae, R., Carrasco, J. M., Busso, G., Burgess, P. W., Cacciari, C., Davidson, M., Harrison, D. L., Hodgkin, S. T., Jordi, C., Osborne, P. J., Pancino, E., Altavilla, G., Barstow, M. A., Bailer-Jones, C. A. L., Bellazzini, M., Brown, A. G. A., Castellani, M., Cowell, S., Delchambre, L., De Luise, F., Diener, C., Fabricius, C., Fouesneau, M., Frémat, Y., Gilmore, G., Giuffrida, G., Hambly, N. C., Hidalgo, S., Holland, G., Kostrzewa-Rutkowska, Z., van Leeuwen, F., Lobel, A., Marinoni, S., Miller, N., Pagani, C., Palaversa, L., Piersimoni, A. M., Pulone, L., Ragaini, S., Rainer, M., Richards, P. J., Rixon, G. T., Ruz-Mieres, D., Sanna, N., Sarro, L. M., Rowell, N., Sordo, R., Walton, N. A., and Yoldas, A. Gaia data release 3 - processing and validation of bp/rp low-resolution spectral data. *A and A*, 674:A2, 2023. doi: 10.1051/0004-6361/202243680. URL <https://doi.org/10.1051/0004-6361/202243680>.
- Michael Deistler, Jan Boelts, Peter Steinbach, Guy Moss, Thomas Moreau, Manuel Gloeckler, Pedro L. C. Rodrigues, Julia Linhart, Janne K. Lappalainen, Benjamin Kurt Miller, Pedro J. Gonçalves, Jan-Matthis Lueckmann, Cornelius Schröder, and Jakob H. Macke. Simulation-based inference: A practical guide, 2025. URL <https://arxiv.org/abs/2508.12939>.
- Charita Dellaporta, Jeremias Knoblauch, Theodoros Damoulas, and François-Xavier Briol. Robust bayesian inference for simulator-based models via the mmd posterior bootstrap. In *International Conference on Artificial Intelligence and Statistics*, pp. 943–970. PMLR, 2022.
- Conor Durkan, Artur Bekasov, Iain Murray, and George Papamakarios. Neural Spline Flows. *arXiv e-prints*, art. arXiv:1906.04032, June 2019. doi: 10.48550/arXiv.1906.04032.
- Conor Durkan, Iain Murray, and George Papamakarios. On contrastive learning for likelihood-free inference. In Hal Daumé III and Aarti Singh (eds.), *Proceedings of the 37th International Conference on Machine Learning*, volume 119 of *Proceedings of Machine Learning Research*, pp. 2771–2781. PMLR, 13–18 Jul 2020. URL <https://proceedings.mlr.press/v119/durkan20a.html>.
- Lasse Elsemüller, Valentin Pratz, Mischa von Krause, Andreas Voss, Paul-Christian Bürkner, and Stefan T. Radev. Does unsupervised domain adaptation improve the robustness of amortized bayesian inference? a systematic evaluation, 2025. URL <https://arxiv.org/abs/2502.04949>.

- 
- David T Frazier and Christopher Drovandi. Robust approximate bayesian inference with synthetic likelihood. *Journal of Computational and Graphical Statistics*, 30(4):958–976, 2021.
- David T. Frazier, Christian P. Robert, and Judith Rousseau. Model misspecification in approximate bayesian computation: Consequences and diagnostics. *Journal of the Royal Statistical Society Series B: Statistical Methodology*, 82(2):421–444, 01 2020. ISSN 1369-7412. doi: 10.1111/rssb.12356. URL <https://doi.org/10.1111/rssb.12356>.
- David T. Frazier, David J. Nott, and Christopher Drovandi and. Synthetic likelihood in misspecified models. *Journal of the American Statistical Association*, 0(0):1–12, 2024. doi: 10.1080/01621459.2024.2370594. URL <https://doi.org/10.1080/01621459.2024.2370594>.
- Masahiro Fujisawa, Takeshi Teshima, Issei Sato, and Masashi Sugiyama.  $\gamma$ -abc: Outlier-robust approximate bayesian computation based on a robust divergence estimator. In *International Conference on Artificial Intelligence and Statistics*, pp. 1783–1791. PMLR, 2021.
- Gaia Collaboration. The Gaia mission. *aap*, 595:A1, November 2016. doi: 10.1051/0004-6361/201629272.
- Manuel Glöckler, Michael Deistler, and Jakob H. Macke. Variational methods for simulation-based inference. In *International Conference on Learning Representations*, 2022. URL <https://openreview.net/forum?id=kZOUYdhqkNY>.
- Manuel Glöckler, Michael Deistler, and Jakob H. Macke. Adversarial robustness of amortized Bayesian inference. *arXiv e-prints*, art. arXiv:2305.14984, May 2023. doi: 10.48550/arXiv.2305.14984.
- Manuel Glöckler, Michael Deistler, Christian Dietrich Weilbach, Frank Wood, and Jakob H. Macke. All-in-one simulation-based inference. In *ICML*, 2024. URL <https://openreview.net/forum?id=DL79HYCFFq>.
- David Greenberg, Marcel Nonnenmacher, and Jakob Macke. Automatic posterior transformation for likelihood-free inference. In *International conference on machine learning*, pp. 2404–2414. PMLR, 2019.
- Meysam Hashemi, Abolfazl Ziaemehr, Marmaduke M. Woodman, Jan Fousek, Spase Petkoski, and Viktor K. Jirsa. Simulation-based inference on virtual brain models of disorders. *Machine Learning: Science and Technology*, 5(3):035019, September 2024. doi: 10.1088/2632-2153/ad6230.
- Joeri Hermans, Volodimir Begy, and Gilles Louppe. Likelihood-free mcmc with amortized approximate ratio estimators. In *International conference on machine learning*, pp. 4239–4248. PMLR, 2020.
- Joeri Hermans, Arnaud Delaunoy, François Rozet, Antoine Wehenkel, Volodimir Begy, and Gilles Louppe. A crisis in simulation-based inference? beware, your posterior approximations can be unfaithful. *Transactions on Machine Learning Research*, 2022. ISSN 2835-8856. URL <https://openreview.net/forum?id=LHAbHkt6Aq>.
- R Devon Hjelm, Alex Fedorov, Samuel Lavoie-Marchildon, Karan Grewal, Phil Bachman, Adam Trischler, and Yoshua Bengio. Learning deep representations by mutual information estimation and maximization. In *International Conference on Learning Representations*, 2019. URL <https://openreview.net/forum?id=Bklr3j0cKX>.
- Bowen Huang, Haibo Yuan, Maosheng Xiang, Yang Huang, Kai Xiao, Shuai Xu, Ruoyi Zhang, Lin Yang, Zexi Niu, and Hongrui Gu. A comprehensive correction of the gaia dr3 xp spectra. *The Astrophysical Journal Supplement Series*, 271(1):13, feb 2024. doi: 10.3847/1538-4365/ad18b1. URL <https://dx.doi.org/10.3847/1538-4365/ad18b1>.
- Daolang Huang, Ayush Bharti, Amauri Souza, Luigi Acerbi, and Samuel Kaski. Learning robust statistics for simulation-based inference under model misspecification. *Advances in Neural Information Processing Systems*, 36:7289–7310, 2023.
- Rob J. Hyndman. Computing and graphing highest density regions. *The American Statistician*, 50(2): 120–126, 1996. doi: 10.2307/2684423. URL <https://doi.org/10.2307/2684423>.

- 
- Rafael Izbicki, Ann Lee, and Chad Schafer. High-Dimensional Density Ratio Estimation with Extensions to Approximate Likelihood Computation. In Samuel Kaski and Jukka Corander (eds.), *Proceedings of the Seventeenth International Conference on Artificial Intelligence and Statistics*, volume 33 of *Proceedings of Machine Learning Research*, pp. 420–429, Reykjavik, Iceland, 22–25 Apr 2014. PMLR. URL <https://proceedings.mlr.press/v33/izbicki14.html>.
- Ryan P. Kelly, David J Nott, David Tyler Frazier, David J Warne, and Christopher Drovandi. Misspecification-robust sequential neural likelihood for simulation-based inference. *Transactions on Machine Learning Research*, 2024. ISSN 2835-8856. URL <https://openreview.net/forum?id=tb0YJwXhcY>.
- Ryan P Kelly, David J Warne, David T Frazier, David J Nott, Michael U Gutmann, and Christopher Drovandi. Simulation-based bayesian inference under model misspecification. *arXiv preprint arXiv:2503.12315*, 2025.
- Diederik P Kingma and Max Welling. Auto-encoding variational bayes. *arXiv preprint arXiv:1312.6114*, 2013.
- Pablo Lemos, Miles Cranmer, Muntazir Abidi, ChangHoon Hahn, Michael Eickenberg, Elena Massara, David Yallup, and Shirley Ho. Robust simulation-based inference in cosmology with bayesian neural networks. *Machine Learning: Science and Technology*, 4(1):01LT01, February 2023. ISSN 2632-2153. doi: 10.1088/2632-2153/acbb53. URL <http://dx.doi.org/10.1088/2632-2153/acbb53>.
- Jan-Matthis Lueckmann, Pedro J Goncalves, Giacomo Bassetto, Kaan Öcal, Marcel Nonnenmacher, and Jakob H Macke. Flexible statistical inference for mechanistic models of neural dynamics. In I. Guyon, U. Von Luxburg, S. Bengio, H. Wallach, R. Fergus, S. Vishwanathan, and R. Garnett (eds.), *Advances in Neural Information Processing Systems*, volume 30. Curran Associates, Inc., 2017. URL [https://proceedings.neurips.cc/paper\\_files/paper/2017/file/addfa9b7e234254d26e9c7f2af1005cb-Paper.pdf](https://proceedings.neurips.cc/paper_files/paper/2017/file/addfa9b7e234254d26e9c7f2af1005cb-Paper.pdf).
- Jan-Matthis Lueckmann, Giacomo Bassetto, Theofanis Karaletsos, and Jakob H. Macke. Likelihood-free inference with emulator networks. In Francisco Ruiz, Cheng Zhang, Dawen Liang, and Thang Bui (eds.), *Proceedings of The 1st Symposium on Advances in Approximate Bayesian Inference*, volume 96 of *Proceedings of Machine Learning Research*, pp. 32–53. PMLR, 02 Dec 2019. URL <https://proceedings.mlr.press/v96/lueckmann19a.html>.
- Charles C Margossian and David M Blei. Amortized variational inference: When and why? *arXiv preprint arXiv:2307.11018*, 2023.
- Orazio Miglino, Henrik Hautop Lund, and Stefano Nolfi. Evolving mobile robots in simulated and real environments. *Artificial life*, 2(4):417–434, 1995.
- Aayush Mishra, Daniel Habermann, Marvin Schmitt, Stefan T. Radev, and Paul-Christian Bürkner. Robust amortized bayesian inference with self-consistency losses on unlabeled data. In *Frontiers in Probabilistic Inference: Learning meets Sampling*, 2025. URL <https://openreview.net/forum?id=RwKyg5BcgN>.
- Siddharth Mishra-Sharma and Kyle Cranmer. Neural simulation-based inference approach for characterizing the galactic center  $\gamma$ -ray excess. *Phys. Rev. D*, 105:063017, Mar 2022. doi: 10.1103/PhysRevD.105.063017. URL <https://link.aps.org/doi/10.1103/PhysRevD.105.063017>.
- Montegriffo, P., De Angeli, F., Andrae, R., Riello, M., Pancino, E., Sanna, N., Bellazzini, M., Evans, D. W., Carrasco, J. M., Sordo, R., Busso, G., Cacciari, C., Jordi, C., van Leeuwen, F., Vallenari, A., Altavilla, G., Barstow, M. A., Brown, A. G. A., Burgess, P. W., Castellani, M., Cowell, S., Davidson, M., De Luise, F., Delchambre, L., Diener, C., Fabricius, C., Frémat, Y., Fouesneau, M., Gilmore, G., Giuffrida, G., Hambly, N. C., Harrison, D. L., Hidalgo, S., Hodgkin, S. T., Holland, G., Marinoni, S., Osborne, P. J., Pagani, C., Palaversa, L., Piersimoni, A. M., Pulone, L., Ragaini, S., Rainer, M., Richards, P. J., Rowell, N., Ruz-Mieres, D., Sarro, L. M., Walton, N. A., and Yoldas, A. Gaia data release 3 - external calibration of bp/rp low-resolution spectroscopic data. *A and A*, 674:A3, 2023. doi: 10.1051/0004-6361/202243880. URL <https://doi.org/10.1051/0004-6361/202243880>.

- 
- Mayank Nautiyal, Andrey Shternshis, Andreas Hellander, and Prashant Singh. Variational autoencoders for efficient simulation-based inference. *arXiv preprint arXiv:2411.14511*, 2024.
- Radford Neal. MCMC Using Hamiltonian Dynamics. In *Handbook of Markov Chain Monte Carlo*, pp. 113–162. Chapman and Hall/CRC, 2011. doi: 10.1201/b10905.
- Matthew O’Callaghan, Gerry Gilmore, and Kaisey S. Mandel. Quantifying interstellar extinction at high Galactic latitudes. *MNRAS*, 535(3):2149–2172, December 2024. doi: 10.1093/mnras/stae2397.
- Jonathan Oesterle, Christian Behrens, Cornelius Schröder, Thoralf Hermann, Thomas Euler, Katrin Franke, Robert G Smith, Günther Zeck, and Philipp Berens. Bayesian inference for biophysical neuron models enables stimulus optimization for retinal neuroprosthetics. *eLife*, 9:e54997, oct 2020. ISSN 2050-084X. doi: 10.7554/eLife.54997. URL <https://doi.org/10.7554/eLife.54997>.
- George Papamakarios and Iain Murray. Fast epsilon-free inference of simulation models with bayesian conditional density estimation. In D. Lee, M. Sugiyama, U. Luxburg, I. Guyon, and R. Garnett (eds.), *Advances in Neural Information Processing Systems*, volume 29. Curran Associates, Inc., 2016. URL [https://proceedings.neurips.cc/paper\\_files/paper/2016/file/6aca97005c68f1206823815f66102863-Paper.pdf](https://proceedings.neurips.cc/paper_files/paper/2016/file/6aca97005c68f1206823815f66102863-Paper.pdf).
- George Papamakarios, Theo Pavlakou, and Iain Murray. Masked autoregressive flow for density estimation, 2018. URL <https://arxiv.org/abs/1705.07057>.
- George Papamakarios, David Sterratt, and Iain Murray. Sequential neural likelihood: Fast likelihood-free inference with autoregressive flows. In *The 22nd international conference on artificial intelligence and statistics*, pp. 837–848. PMLR, 2019.
- L. F. Price, C. C. Drovandi, A. Lee, and D. J. Nott. Bayesian synthetic likelihood. *Journal of Computational and Graphical Statistics*, 27(1):1–11, 2018. doi: 10.1080/10618600.2017.1302882. URL <https://doi.org/10.1080/10618600.2017.1302882>.
- Donald B. Rubin. Bayesianly Justifiable and Relevant Frequency Calculations for the Applied Statistician. *The Annals of Statistics*, 12(4):1151 – 1172, 1984. doi: 10.1214/aos/1176346785. URL <https://doi.org/10.1214/aos/1176346785>.
- Donald B. Rubin. The calculation of posterior distributions by data augmentation: Comment: A non-iterative sampling/importance resampling alternative to the data augmentation algorithm for creating a few imputations when fractions of missing information are modest: The sir algorithm. *Journal of the American Statistical Association*, 82(398):543–546, 1987. doi: 10.2307/2289460. URL <https://doi.org/10.2307/2289460>.
- Marvin Schmitt, Paul-Christian Bürkner, Ullrich Köthe, and Stefan T. Radev. Detecting model misspecification in amortized bayesian inference with neural networks: An extended investigation. *CoRR*, abs/2406.03154, 2024. URL <https://doi.org/10.48550/arXiv.2406.03154>.
- Jack Simons, Song Liu, and Mark Beaumont. Variational likelihood-free gradient descent. In *Fourth Symposium on Advances in Approximate Bayesian Inference*, 2022. URL <https://openreview.net/forum?id=svH3klEbuXa>.
- Paxson Swierc, Marcos Tamargo-Arizmendi, Aleksandra Ćiprijanović, and Brian D Nord. Domain-adaptive neural posterior estimation for strong gravitational lens analysis. *arXiv preprint arXiv:2410.16347*, 2024.
- The Atlas Collaboration. An implementation of neural simulation-based inference for parameter estimation in ATLAS. *Reports on Progress in Physics*, 88(6):067801, June 2025. doi: 10.1088/1361-6633/add370.
- George Tucker, Dieterich Lawson, Shixiang Gu, and Chris J Maddison. Doubly reparameterized gradient estimators for monte carlo objectives. *arXiv preprint arXiv:1810.04152*, 2018.
- Wang. The Value-added Catalog for LAMOST DR8 Low-resolution Spectra. *apjs*, 259(2):51, April 2022. doi: 10.3847/1538-4365/ac4df7.

---

Daniel Ward, Patrick Cannon, Mark Beaumont, Matteo Fasiolo, and Sebastian Schmon. Robust neural posterior estimation and statistical model criticism. *Advances in Neural Information Processing Systems*, 35:33845–33859, 2022.

Antoine Wehenkel, Juan L. Gamella, Ozan Sener, Jens Behrmann, Guillermo Sapiro, Joern-Henrik Jacobsen, and marco cuturi. Addressing misspecification in simulation-based inference through data-driven calibration. In *Forty-second International Conference on Machine Learning*, 2025. URL <https://openreview.net/forum?id=y3d4Bs2r7r>.

Samuel Wiqvist, Jes Frelsen, and Umberto Picchini. Sequential neural posterior and likelihood approximation. *arXiv preprint arXiv:2102.06522*, 2021.

Callum E. C. Witten, David S. Aguado, Jason L. Sanders, Vasily Belokurov, N. Wyn Evans, Sergey E. Kuposov, Carlos Allende Prieto, Francesca De Angeli, and Mike J. Irwin. Information content of BP/RP spectra in Gaia DR3. *MNRAS*, 516(3):3254–3265, November 2022. doi: 10.1093/mnras/stac2273.

Justine Zeghal, Denise Lanzieri, François Lanusse, Alexandre Boucaud, Gilles Louppe, Eric Aubourg, Adrian E. Bayer, and The LSST Dark Energy Science Collaboration. Simulation-based inference benchmark for lsst weak lensing cosmology, 2024. URL <https://arxiv.org/abs/2409.17975>.

## A Appendix

In this section, we discuss some results that are not central to the main claims of the paper.

### A.1 Sample importance resampling for Spectra task well-specified

Sample-importance-resampling is a useful technique in variational autoencoder frameworks, as it adjusts the variational posterior samples based on the learnt forward model. In Figure 7, we show an example of the effect of sample-importance-resampling in the spectra task. From this plot, it is clear that the samples from the variational posterior (green) are sampled in regions of parameter space with extremely low prior probability. The sample-importance-resampling has the effect of tightening the posterior by removing points which are incompatible with the prior and the simulator model.

## Spectra Task (Well-specified)

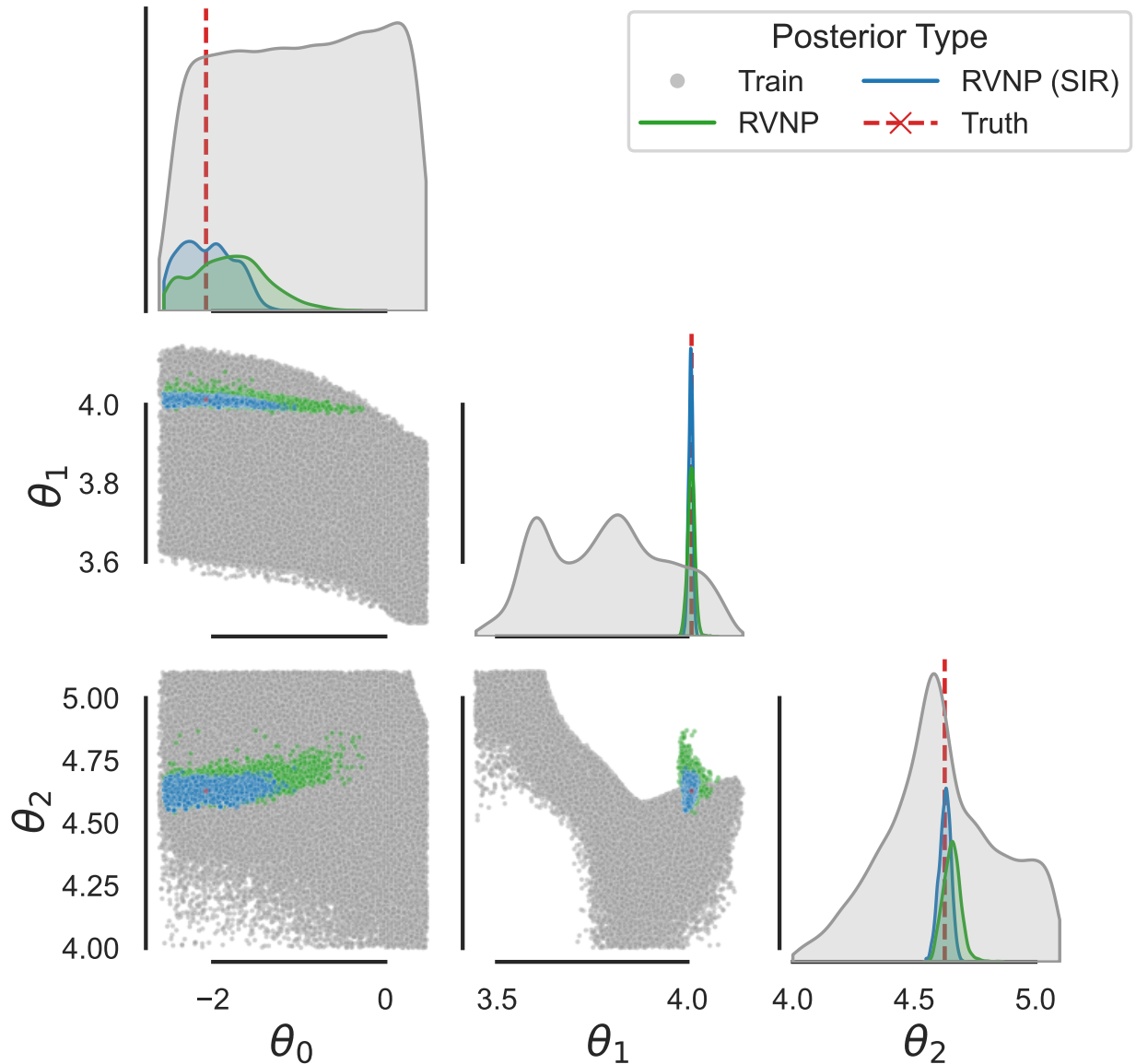


Figure 7: (SIR) indicates sample-importance-resampling. We show the effect of sample-importance-resampling on the well-specified spectra task. The effect largely reduces the number of points which have very low prior probability and are incompatible with the simulator likelihood proxy.

### A.2 Well-specified case

In this subsection, we present plots of the metrics when we use RVNP to infer the posterior distribution when the model is well-specified. We find that RVNP is not significantly detrimental to posterior recovery in the well-specified case, as it will become under-confident and the sample-importance-resampling distribution becomes very close to the NPE estimate. RVNP is quite under-confident in the spectra and pendulum task. However, this is highly preferable to overconfidence. Moreover, the NPE task is highly over-fit in both of these tasks, and even a small perturbation in output space will give highly wrong posteriors. Such a tight posterior would rarely be used in practice.

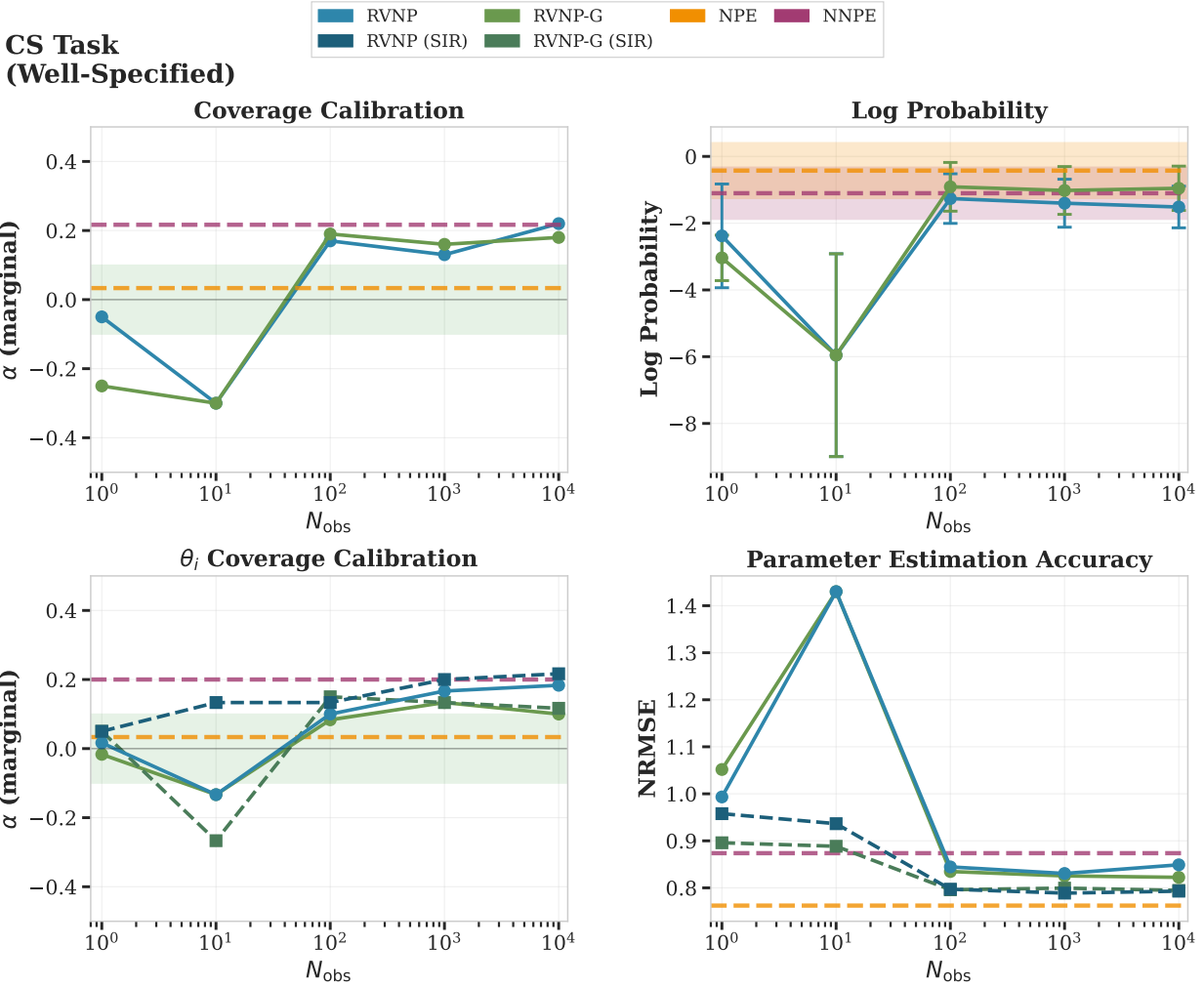


Figure 8: Results for the well-specified CS task. We conclude that RVNP and its variants can recover robust posterior inference in amortised simulation-based inference when the simulator is well specified. However, the error introduced by the error model will inflate the posterior. Sample-importance-resampling will sample closest to the NPE estimate. The hue in the middle plots indicates the error bar on the NPE and NNPE algorithms. For  $\alpha$  nearest to 0 is best, with positive values representing underconfidence and negative values representing overconfidence. For the log-probability, higher values are better. For NRMSE, lower values are better. (SIR) indicates sample-importance-resampling.

**Results.**

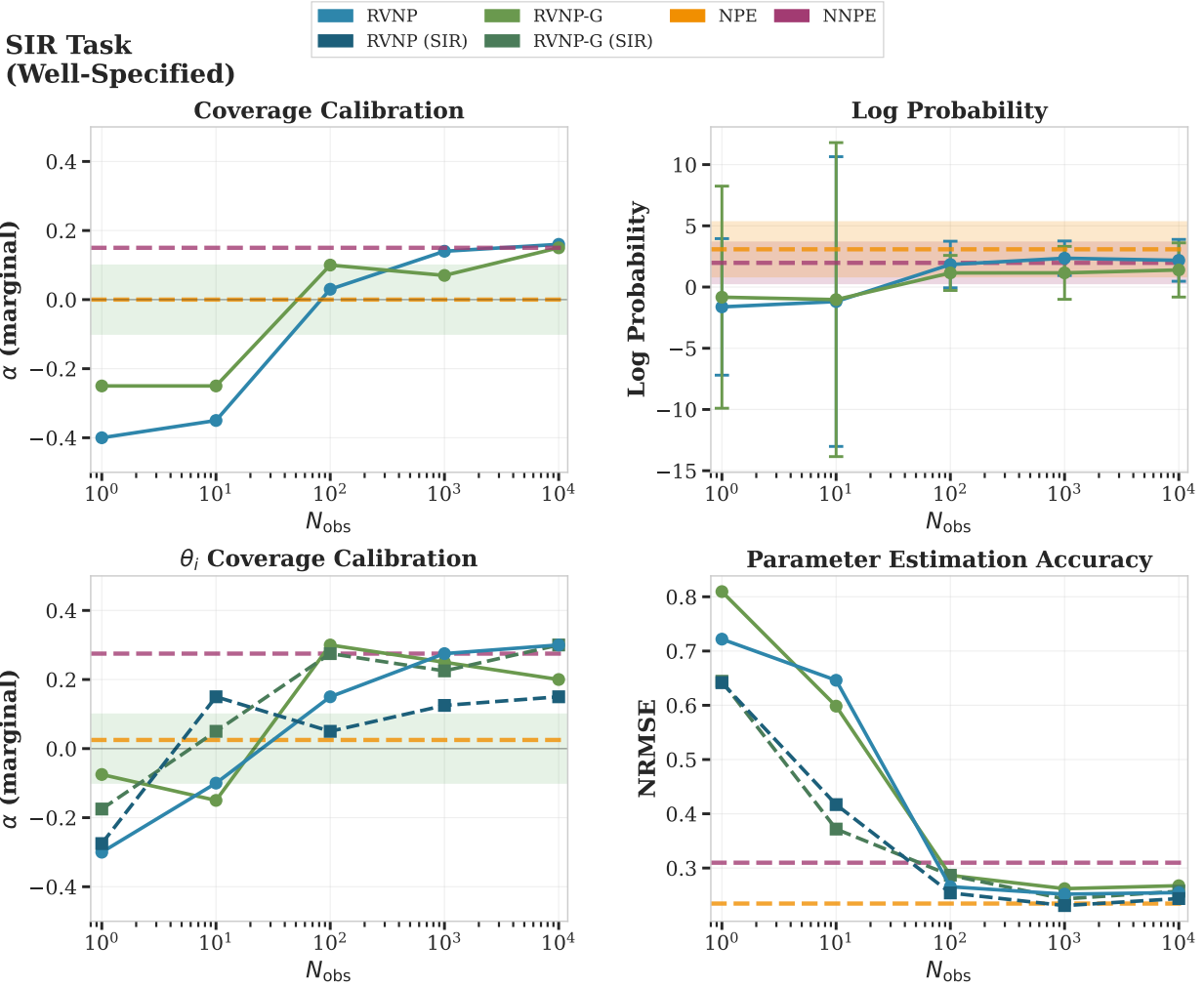


Figure 9: Results for the well-specified SIR task. We conclude that RVNP and its variants can recover robust posterior inference in amortised simulation-based inference when the model is well-specified. However, the error introduced by the error model will inflate the posterior. Sample-importance-resampling will sample closest to the NPE estimate, and hybrid sample importance-resampling matches the NRMSE of the NPE. The hue in the middle plots indicates the error bar on the NPE and NNPE algorithms. For  $\alpha$  nearest to 0 is best, with positive values representing underconfidence and negative values representing overconfidence. For the log-probability, higher values are better. For NRMSE, lower values are better. (SIR) indicates sample-importance-resampling and should not be confused with the SIR Task.

## Results.

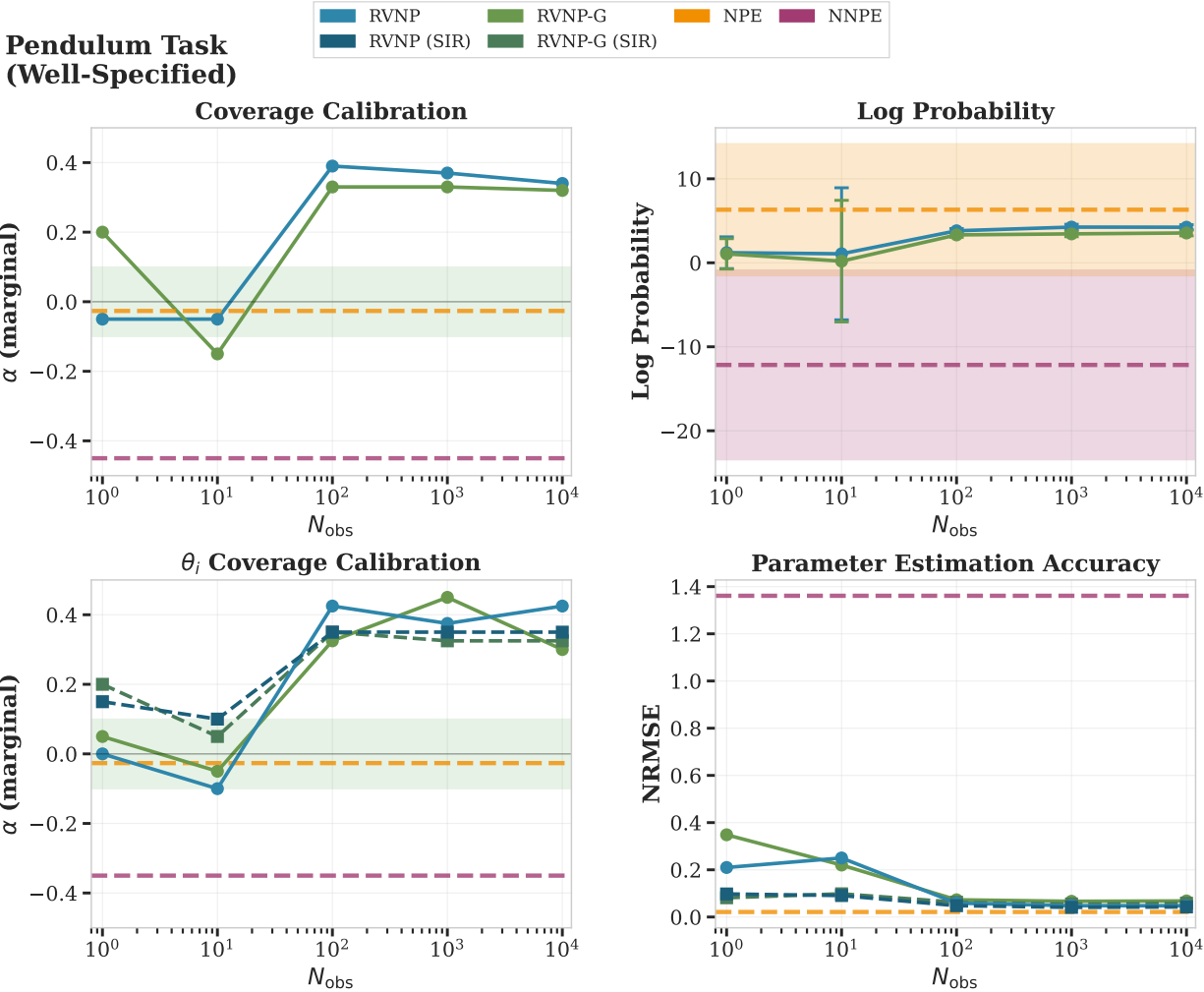


Figure 10: Results for the well-specified Pendulum task. We conclude that RVNP and its variants can recover robust posterior inference in amortised simulation-based inference when the model is well-specified. The hue in the middle plots indicates the error bar on the NPE and NNPE algorithms. For  $\alpha$  nearest to 0 is best, with positive values representing underconfidence and negative values representing overconfidence. For the log-probability, higher values are better. For NRMSE, lower values are better. (SIR) indicates sample-importance-resampling

**Results.**

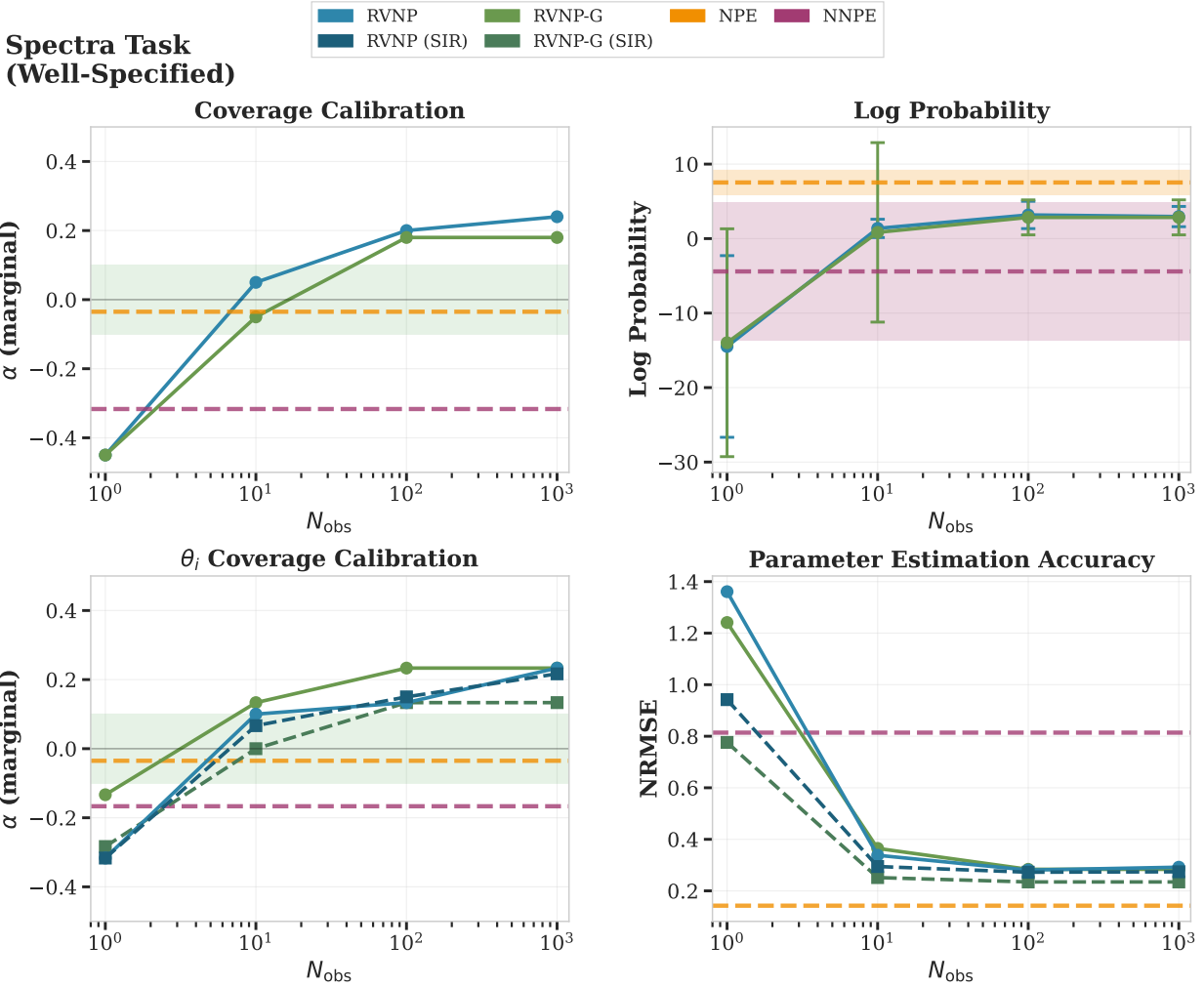


Figure 11: Results for the well-specified spectra task. We conclude that RVNP and its variants can recover robust posterior inference in amortised simulation-based inference. The hue in the middle plots indicates the error bar on the NPE and NNPE algorithms. For  $\alpha$  nearest to 0 is best, with positive values representing underconfidence and negative values representing overconfidence. For the log-probability, higher values are better. For NRMSE, lower values are better. (SIR) indicates sample-importance-resampling

### A.3 Learnt Error Model for $N_{\text{obs}} = 1000$ in final two summary statistics

We display the final two dimensions of the output of the simulator in each of the tasks.

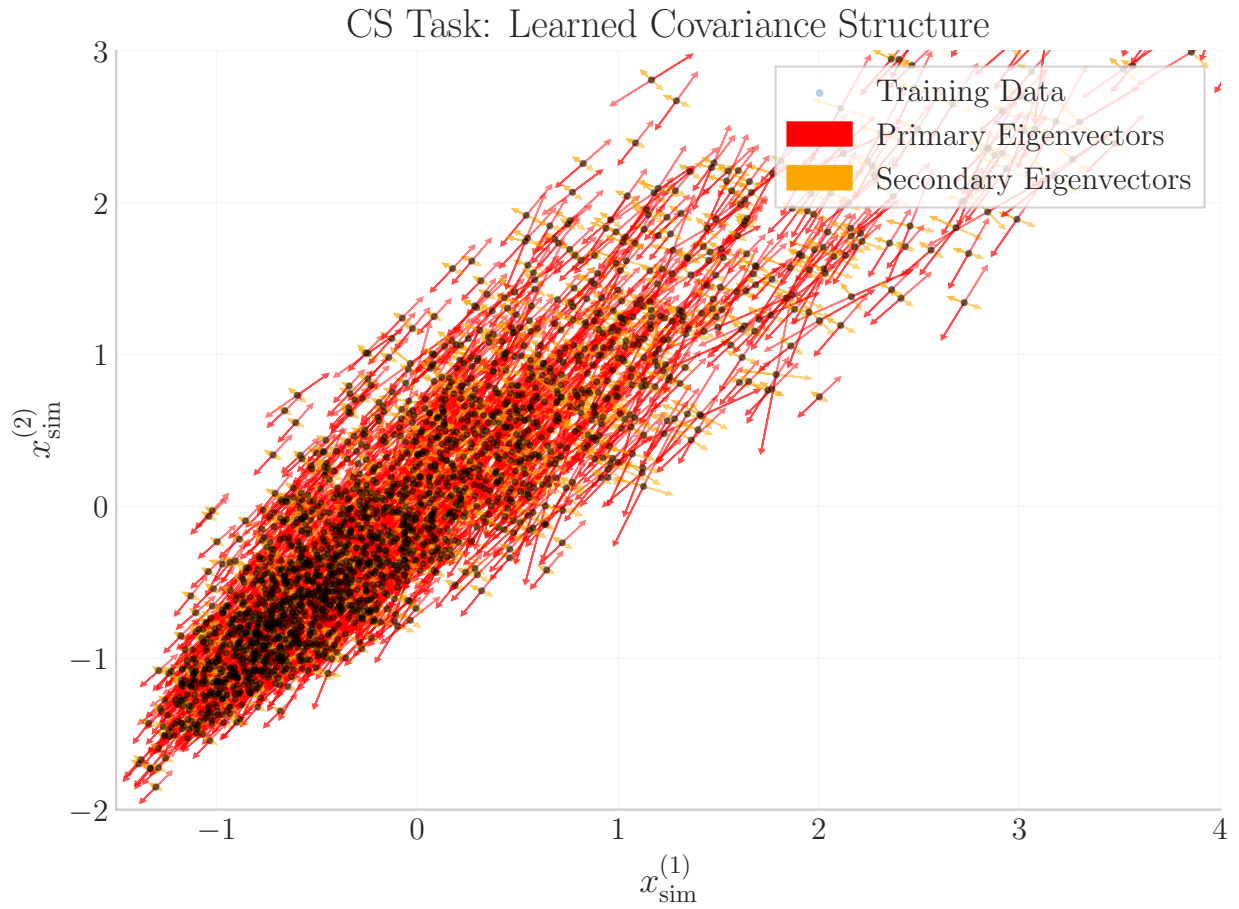


Figure 12: The final two dimensions of the output of the simulator in the CS task, with the bars indicating the direction of the eigenvectors of the covariance matrix in this subspace. After clipping the lengths of the vectors above a magnitude of 1 to ignore outliers, the lengths have been scaled to a maximum length of 0.3 relative to each other.

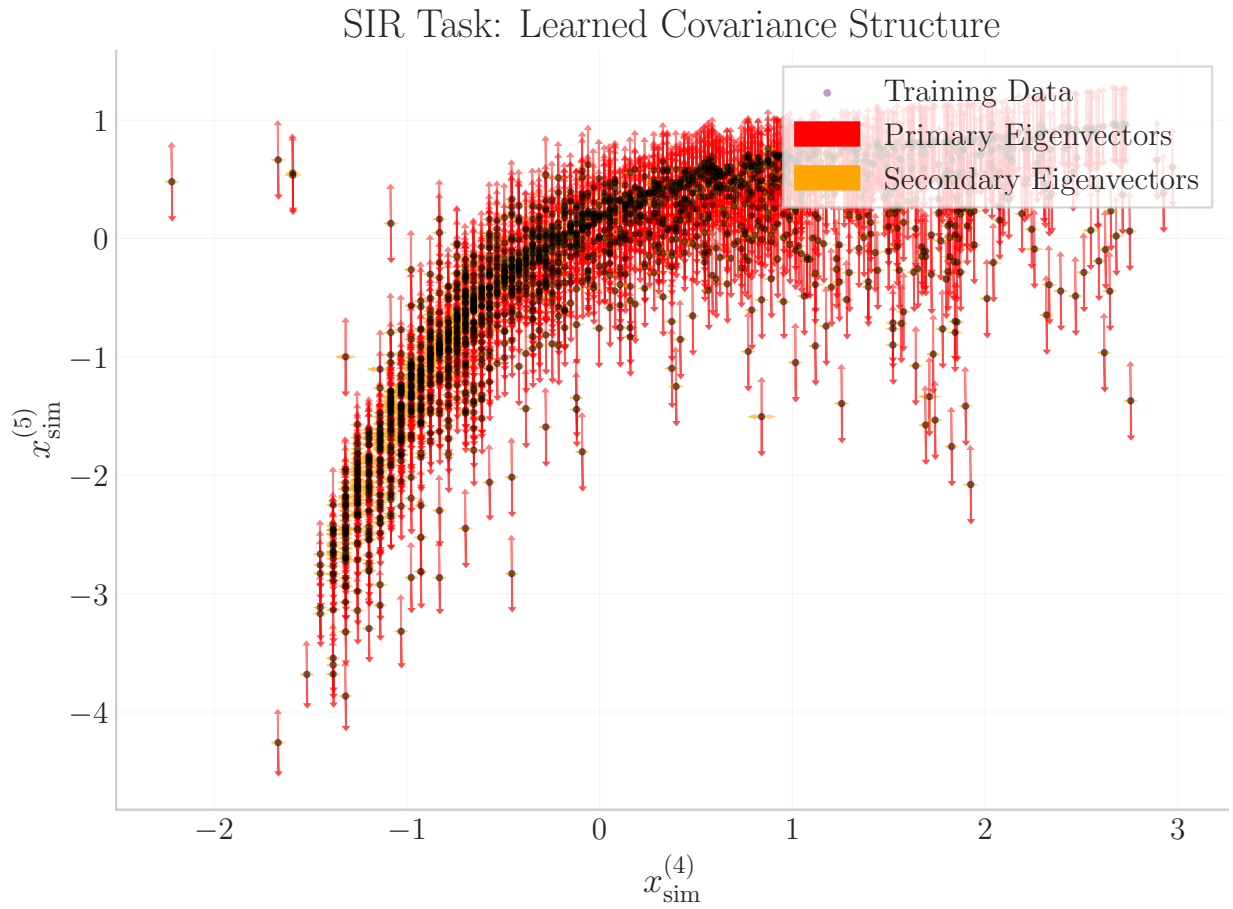


Figure 13: The final two dimensions of the output of the simulator in the SIR task, with the bars indicating the direction of the eigenvectors of the covariance matrix in this subspace. After clipping the lengths of the vectors above a magnitude of 5 to ignore outliers, the lengths have been scaled to a maximum length of 0.3 relative to each other.

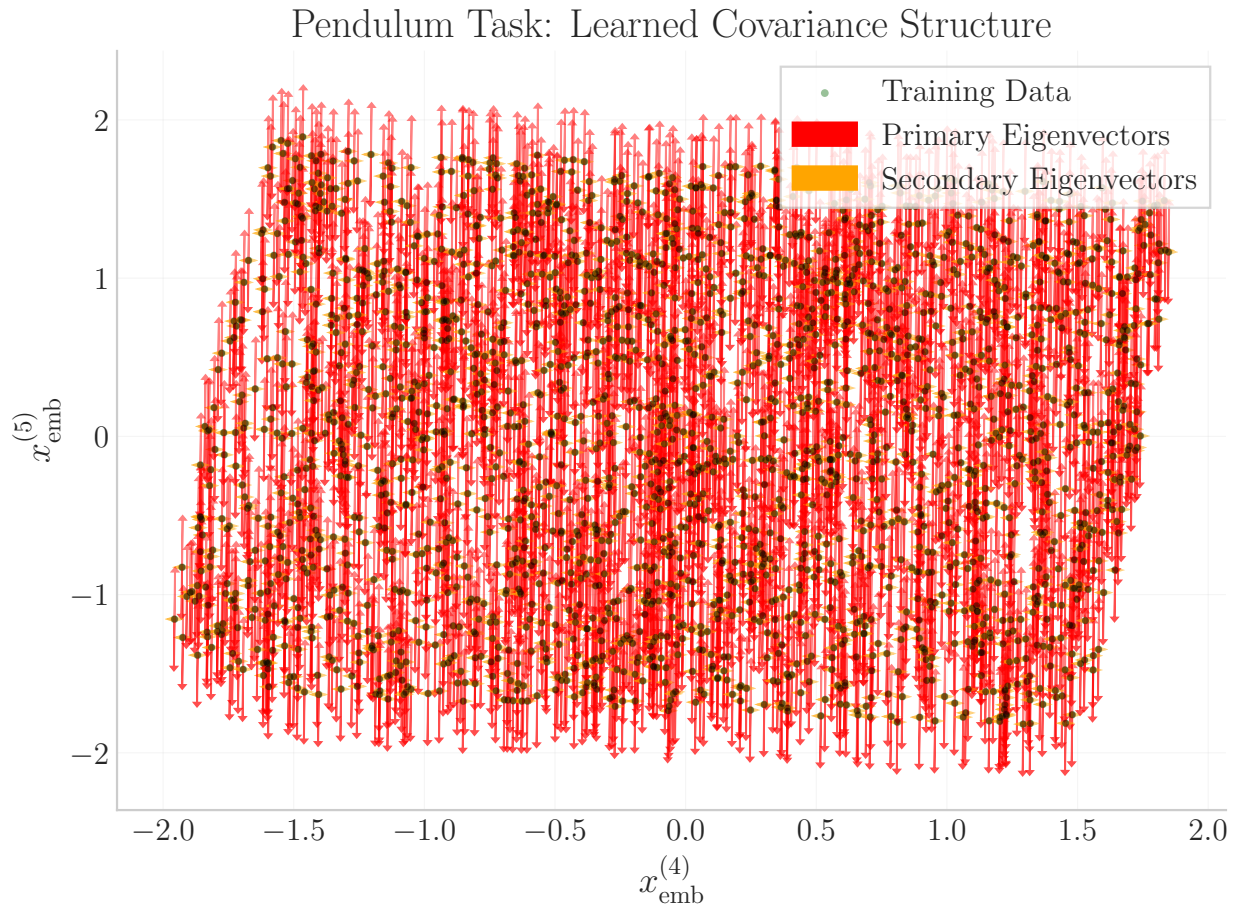


Figure 14: The final two dimensions of the output of the simulator in the SIR task, with the bars indicating the direction of the eigenvectors of the covariance matrix in this subspace. After clipping the lengths of the vectors above a magnitude of 1 to ignore outliers, the lengths have been scaled to a maximum length of 0.3 relative to each other.

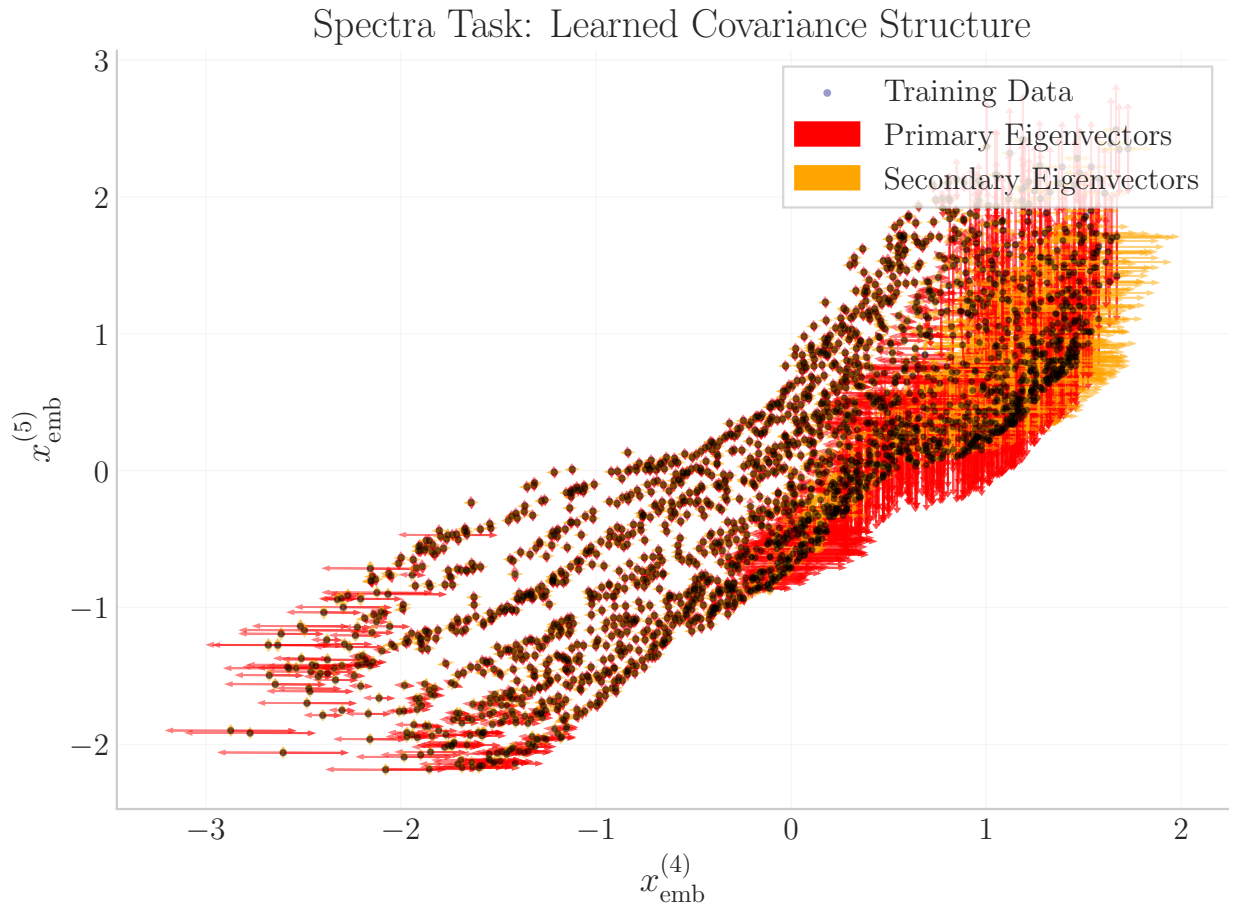


Figure 15: The final two dimensions of the output of the simulator in the SIR task, with the bars indicating the direction of the eigenvectors of the covariance matrix in this subspace. After clipping the lengths of the vectors above a magnitude of 1 to ignore outliers, the lengths have been scaled to a maximum length of 0.3 relative to each other.

#### A.4 Misspecified Observations Overlaying Training Simulations

Here, we display the simulated samples and the misspecified points together for each task.

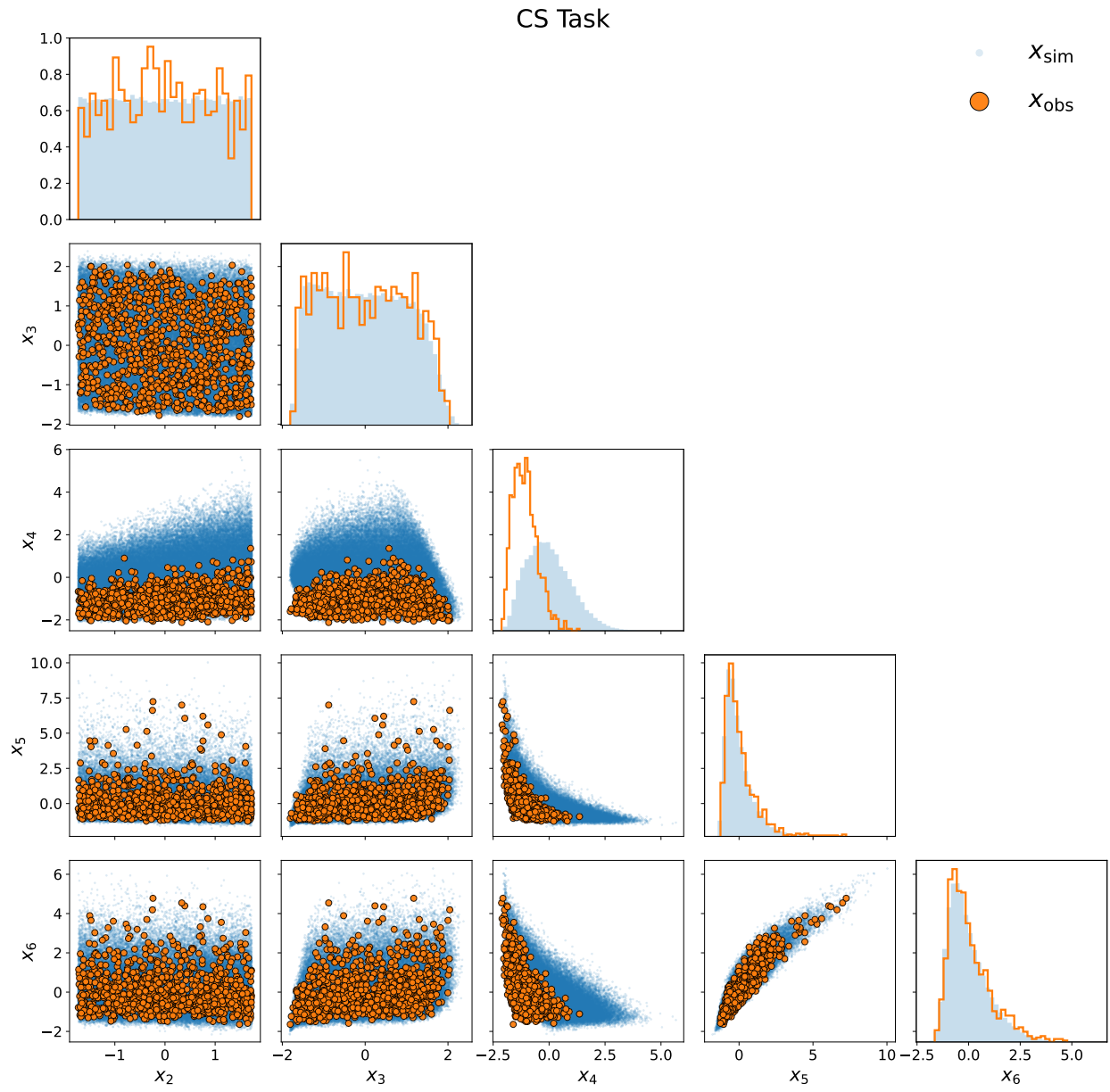


Figure 16: The simulated samples and the misspecified points for the CS Task.

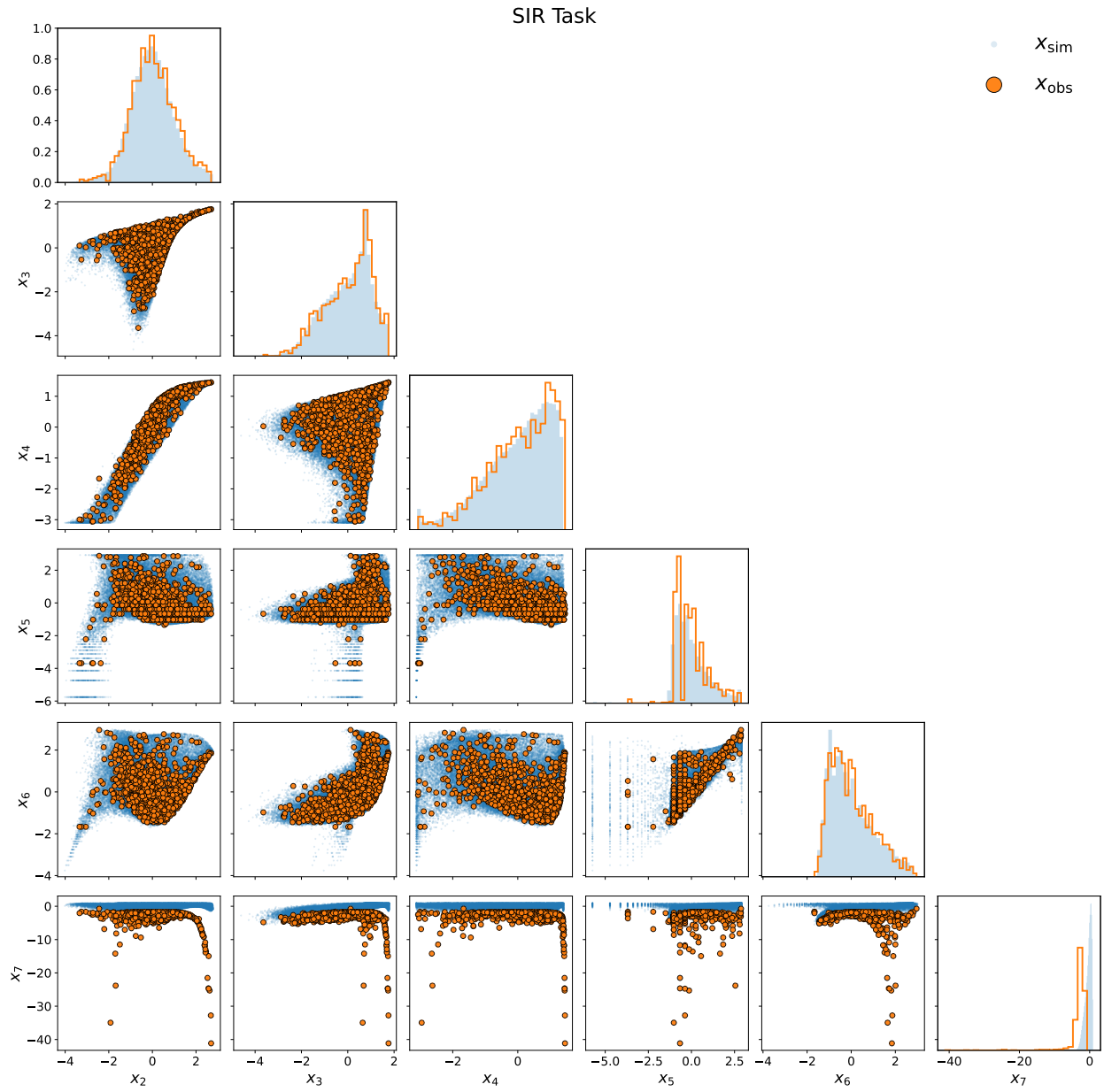


Figure 17: The simulated samples and the misspecified points for the SIR Task.

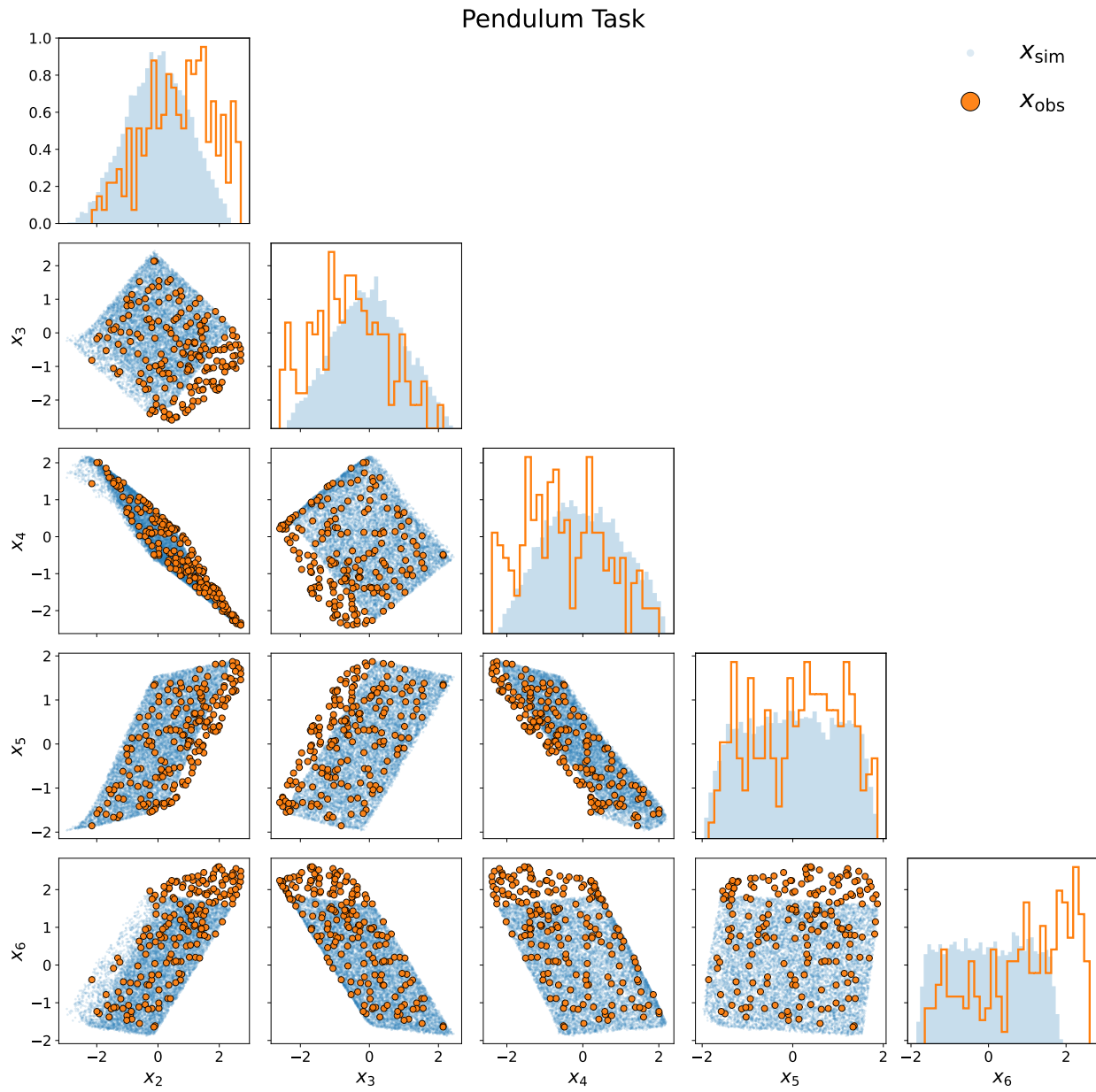


Figure 18: The simulated samples and the misspecified points for the Pendulum Task.

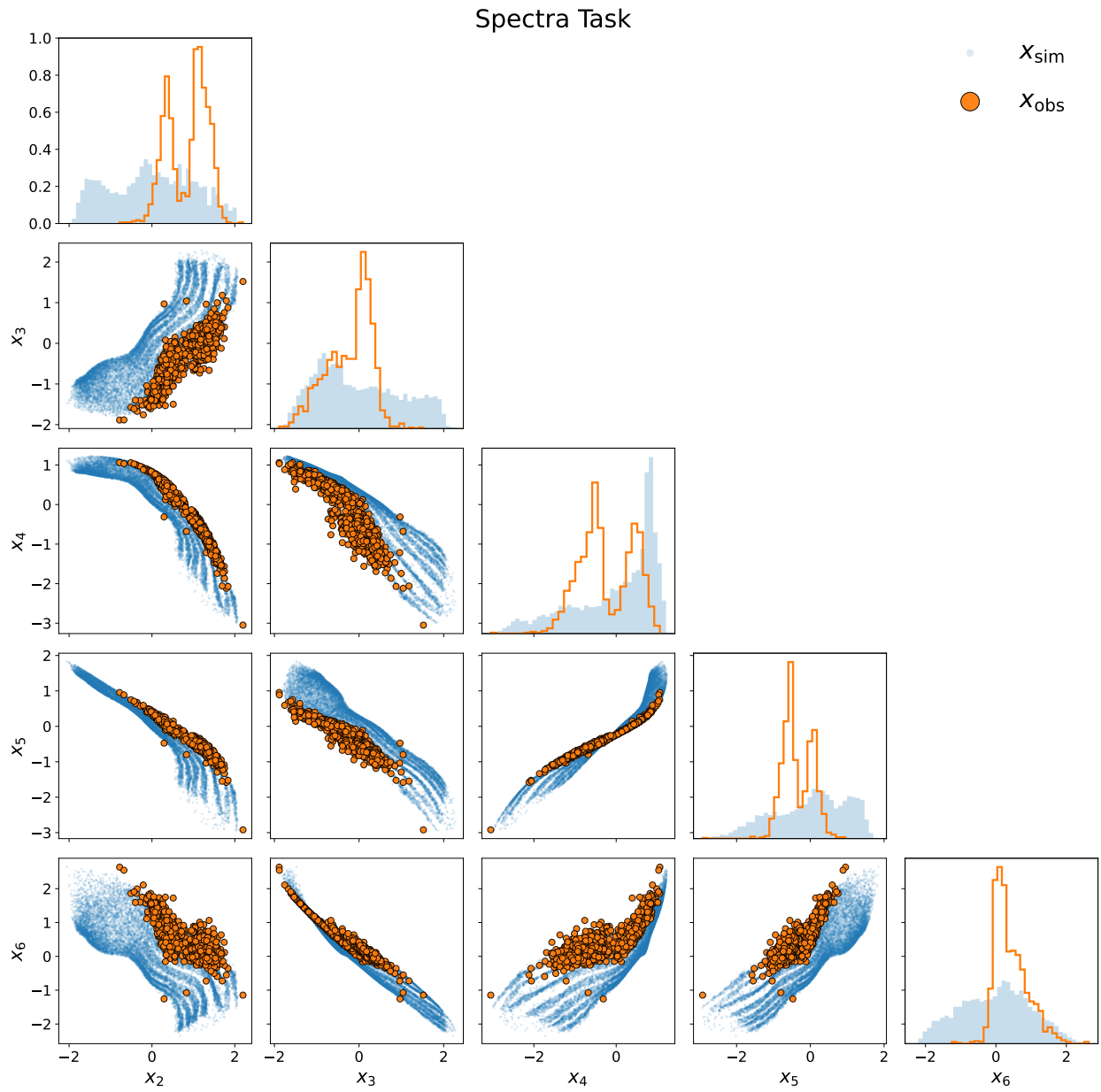


Figure 19: The simulated samples and the misspecified points for the Spectra Task.

## A.5 RVNP Training Pipeline

We provide an overview of the RVNP training pipeline in the following algorithms.

---

**Algorithm 1** Robust Variational Neural Posterior Estimation (RVNP)

---

```
1: PretrainLikelihood( $D = \{(\mathbf{x}_{\text{sim}}, \boldsymbol{\theta})\}$ )
2: repeat
3:   Sample minibatch  $B \subset D$ 
4:    $\mathcal{L}_{\text{NLE}}(\boldsymbol{\Psi}) \leftarrow -\mathbb{E}_B[\log p_{\boldsymbol{\Psi}}(\mathbf{x}_{\text{sim}} | \boldsymbol{\theta})]$ 
5:    $\boldsymbol{\Psi} \leftarrow \boldsymbol{\Psi} - \eta \nabla_{\boldsymbol{\Psi}} \mathcal{L}_{\text{NLE}}$ 
6: until convergence
7: return  $p_{\boldsymbol{\Psi}^*}(\mathbf{x}_{\text{sim}} | \boldsymbol{\theta})$ 
8:
9: LearnPosteriorAndErrorModel( $p_{\boldsymbol{\Psi}^*}, \mathcal{O} = \{\mathbf{x}_{\text{obs}}\}$ )
10: repeat
11:   for each  $\mathbf{x}_{\text{obs}} \in$  minibatch  $\mathcal{O}$  do
12:      $\{\boldsymbol{\theta}^{(l)}\}_{l=1}^K \sim q_{\phi}(\boldsymbol{\theta} | \mathbf{x}_{\text{obs}})$ 
13:     for  $l = 1$  to  $K$  do
14:        $\{\mathbf{x}_{\text{sim}}^{(l,m)}\}_{m=1}^M \sim p_{\boldsymbol{\Psi}^*}(\mathbf{x}_{\text{sim}} | \boldsymbol{\theta}^{(l)})$ 
15:        $w^{(l)} \leftarrow \frac{1}{M} \sum_{m=1}^M \frac{p_{\alpha}(\mathbf{x}_{\text{obs}} | \mathbf{x}_{\text{sim}}^{(l,m)}, \boldsymbol{\theta}^{(l)}) p(\boldsymbol{\theta}^{(l)})}{q_{\phi}(\boldsymbol{\theta}^{(l)} | \mathbf{x}_{\text{obs}})}$ 
16:     end for
17:      $\mathcal{L}_V \leftarrow -\log \left( \frac{1}{K} \sum_{l=1}^K w^{(l)} \right) - \log p(\alpha)$ 
18:      $(\phi, \alpha) \leftarrow (\phi, \alpha) - \eta \nabla_{(\phi, \alpha)} \mathcal{L}_V$ 
19:   end for
20: until convergence
21: return  $q_{\phi^*}(\boldsymbol{\theta} | \mathbf{x}_{\text{obs}}), p_{\alpha^*}(\mathbf{x}_{\text{obs}} | \mathbf{x}_{\text{sim}}, \boldsymbol{\theta})$ 
22:
23: TunePosterior( $q_{\phi^*}, p_{\alpha^*}, D$ ) // Optional: RVNP-T
24: repeat
25:   Sample  $(\mathbf{x}_{\text{sim}}, \boldsymbol{\theta}) \sim D, \mathbf{x}_{\text{obs}} \sim p_{\alpha^*}(\mathbf{x}_{\text{obs}} | \mathbf{x}_{\text{sim}}, \boldsymbol{\theta})$ 
26:    $\mathcal{L}_{\text{tune}}(\phi) \leftarrow -\log q_{\phi}(\boldsymbol{\theta} | \mathbf{x}_{\text{obs}})$ 
27:    $\phi \leftarrow \phi - \eta \nabla_{\phi} \mathcal{L}_{\text{tune}}$ 
28: until convergence
29: return  $q_{\phi^{**}}(\boldsymbol{\theta} | \mathbf{x}_{\text{obs}})$ 
30:
31: Infer( $\mathbf{x}_{\text{obs}}, N_{\text{samples}}$ ) // With optional SIR
32: for  $i = 1$  to  $N_{\text{samples}}$  do
33:    $\boldsymbol{\theta}^{(i)} \sim q_{\phi^*}(\boldsymbol{\theta} | \mathbf{x}_{\text{obs}})$ 
34: end for
35: Optionally apply sample-importance-resampling to  $\{\boldsymbol{\theta}^{(i)}\}$ 
36: return  $\{\boldsymbol{\theta}^{(i)}\}_{i=1}^{N_{\text{samples}}}$ 
```

---

## A.6 Training Procedure

In every task, RVNP is defined using a variational posterior model based on a **rational quadratic spline (RQS) flow** with  $B = 10$  and 15 knots using the masked autoregressive flow architecture template of Papamakarios et al. (2018) and implemented using the `flowjax` python package. The depth of the flow is set to 5 layers, while the neural network conditioner has a hidden block dimension of 52. The flow dimension is the dimension of  $\theta_{\text{dim}}$ , and the conditioning dimension corresponds to that of  $x_{\text{sim}}$ . The simulator flow has the same architecture as the input and output dimensions swapped.

The importance weighted autoencoder objective was trained with a batch size of 1024 over 500 iterations, using the Adam optimiser with a learning rate of  $10^{-3}$ , momentum term  $\beta_1 = 0.9$ ,  $\epsilon = 10^{-8}$ , weight decay  $10^{-5}$ , gradient clipping at 10.0, and a warmup schedule of 1000 steps. Early stopping is applied with a patience of 100 iterations, and 10% of the data is reserved for validation. In the forward modelling of the posterior and the simulator,  $K_{\text{obs samples}} = 30$  is the number of samples used in the importance weighting. In

each task, the simulator was trained using the same optimiser parameters but using the maximum likelihood loss. When sampling with sampling-importance-resampling, we use 5000 particles per observation and sample 100 times per particle.

**Neural Statistic Estimator** To train the neural statistic estimator on the InfoMax objective, we adopt a neural statistic and a discriminator model. We use the same optimiser parameters and batch size for the main training routine. All models are implemented in **Equinox** and trained using JAX. The encoder outputs a deterministic latent representation  $z$  without variational sampling, and the discriminator maximises the mutual information between  $z$  and  $\theta$ . The spectra encoder uses one-dimensional convolutional feature extraction and global attention modelling using a Conformer block. The hidden dimension for both the embeddings and the discriminator is 100. We describe the algorithm in 2.

---

**Algorithm 2** Spectra Encoder Forward Pass

---

**Require:** Input sequence  $x \in \mathbb{R}^{C \times L}$

- 1:  $x \leftarrow \text{GELU}(\text{Conv1}(x))$
- 2:  $x \leftarrow \text{AdaptiveAvgPool}(x)$
- 3:  $x \leftarrow x^\top$  {Prepare for Conformer:  $(C, L) \rightarrow (L, C)$ }
- 4:  $x \leftarrow \text{ConformerBlock}(x)$
- 5:  $x \leftarrow x^\top$  {Back to  $(C, L)$ }
- 6:  $x \leftarrow \text{MeanPool over time}(x)$
- 7:  $x \leftarrow \text{GELU}(\text{fc\_hidden}(x))$
- 8:  $z \leftarrow \text{fc\_out}(x)$
- 9: **return**  $z$

---

The pendulum encoder follows a similar structure but uses a single convolutional layer followed by a Conformer block. (Algorithm 3).

---

**Algorithm 3** Pendulum Encoder Forward Pass

---

**Require:** Input sequence  $x \in \mathbb{R}^{C \times L}$

- 1:  $x \leftarrow \text{GELU}(\text{Conv1}(x))$
- 2:  $x \leftarrow \text{AdaptiveAvgPool}(x)$
- 3:  $x \leftarrow x^\top$
- 4:  $x \leftarrow \text{ConformerBlock}(x)$
- 5:  $x \leftarrow x^\top$
- 6:  $x \leftarrow \text{MeanPool over time}(x)$
- 7:  $z \leftarrow \text{fc\_out}(x)$
- 8: **return**  $z$

---

The discriminator is a simple multilayer perceptron (MLP) that takes the concatenation of the latent embedding  $z$  and conditioning variable  $\theta$  as input, and outputs a scalar logit (Algorithm 4).

---

**Algorithm 4** Discriminator Forward Pass

---

**Require:** Latent embedding  $z \in \mathbb{R}^{d_z}$ , condition vector  $\theta \in \mathbb{R}^{d_\theta}$

- 1:  $x \leftarrow \text{Concat}(z, \theta)$
- 2:  $x \leftarrow \text{ReLU}(\text{fc1}(x))$
- 3:  $x \leftarrow \text{ReLU}(\text{fc2}(x))$
- 4:  $\text{logit} \leftarrow \text{fc3}(x)$
- 5: **return**  $\text{logit}$

---

**InfoMax Loss Function** Chen et al. (2021) show that finding an embedding  $\iota_\omega$  that maximizes the mutual information between  $\theta$  and  $\iota_\omega(\mathbf{x})$  tends towards sufficient statistics of  $\theta$  provided the dimension of

the embedding space is not too small. Furthermore, Hjelm et al. (2019) introduce the InfoMax objective for learning deep representations of high-dimensional data based on maximizing the mutual information. After adopting a discriminator network  $D_\gamma$ , we can generate a lower bound on the mutual information using the Shannon-Jensen divergence

$$\mathcal{I}_{\text{JSD}}(\omega, \gamma) := \mathbb{E}_P[-\text{sp}(-D_\gamma(\theta, \iota_\omega(\mathbf{x})))] - \mathbb{E}_{P \times \tilde{P}}[\text{sp}(D_\gamma(\theta, \iota_\omega(\mathbf{x})))] \tag{24}$$

where  $\text{sp}(u) = \log(1 + e^u)$  is the softplus function,  $P$  is the joint distribution of  $(\theta, \iota_\omega(\mathbf{x}))$ , and  $\tilde{P}$  denotes the product of marginals. Jointly optimizing for the embedding and the discriminator maximises a lower bound on the mutual information. To train the encoders, we maximise the mutual information (MI) between the latent embeddings  $z$  and the conditioning variables  $\theta$ . Algorithm 5 summarises the loss function.

---

**Algorithm 5** InfoMax (Shannon-Jensen) Loss Computation

---

**Require:** Input batch  $x \in \mathbb{R}^{B \times L}$ , real batch  $x_{\text{real}}$ , condition vectors  $\theta \in \mathbb{R}^{B \times d_\theta}$ , encoder  $E(\cdot)$ , discriminator  $D(\cdot)$ , number of shuffles  $S$

- 1: Sample randomness keys for encoder and discriminator
- 2:  $z \leftarrow E(x)$  {Latent embeddings from batch}
- 3:  $z_{\text{real}} \leftarrow E(x_{\text{real}})$  {Latent embeddings from real data}
- 4: Compute joint discriminator outputs:  $l_{\text{joint}} \leftarrow D(z, \theta)$
- 5: Initialise marginal loss accumulator
- 6: **for**  $s = 1 \dots S$  **do**
- 7: Generate random permutation  $\pi_s$  of  $\{1, \dots, B\}$
- 8:  $\theta_{\text{shuffled}} \leftarrow \theta[\pi_s]$
- 9:  $l_{\text{marginal}}^{(s)} \leftarrow D(z, \theta_{\text{shuffled}})$
- 10: Accumulate:  $m^{(s)} \leftarrow -\text{softplus}(l_{\text{marginal}}^{(s)})$
- 11: **end for**
- 12: Compute joint term:  $J \leftarrow -\text{softplus}(-l_{\text{joint}})$
- 13: Compute marginal term:  $M \leftarrow \frac{1}{S} \sum_{s=1}^S m^{(s)}$
- 14: Estimate MI lower bound:  $\hat{I}(z; \theta) \leftarrow \mathbb{E}[J] + \mathbb{E}[M]$
- 15: Shannon loss:  $\mathcal{L}_{\text{Shannon}} \leftarrow -\hat{I}(z; \theta)$
- 16: **return**  $\mathcal{L}_{\text{Shannon}}$

---